

Development of Advanced Methodologies for Three-Dimensional Nanoprinting

By

JOAO FRANCISCO VENTRICI DE SOUZA

B.S. (University of Sao Paulo, Ribeirao Preto, Sao Paulo, Brazil) 2009

M.S. (University of Sao Paulo, Ribeirao Preto, Sao Paulo, Brazil) 2011

DISSERTATION

Submitted in partial satisfaction of the requirements for the degree of

DOCTOR OF PHILOSOPHY

in

Chemistry

in the

OFFICE OF GRADUATE STUDIES

of the

UNIVERSITY OF CALIFORNIA

DAVIS

Approved:

Prof. Gang-yu Liu, Chair

Prof. Tonya Kuhl

Prof. Atul Parikh

Committee in Charge

2017

ProQuest Number: 10618020

All rights reserved

INFORMATION TO ALL USERS

The quality of this reproduction is dependent upon the quality of the copy submitted.

In the unlikely event that the author did not send a complete manuscript and there are missing pages, these will be noted. Also, if material had to be removed, a note will indicate the deletion.



ProQuest 10618020

Published by ProQuest LLC (2017). Copyright of the Dissertation is held by the Author.

All rights reserved.

This work is protected against unauthorized copying under Title 17, United States Code
Microform Edition © ProQuest LLC.

ProQuest LLC.
789 East Eisenhower Parkway
P.O. Box 1346
Ann Arbor, MI 48106 – 1346

Dedicated to Maria Elisabete Darbello Zaniquelli,
exemplary professional and person I wish to mirror.

ACKNOWLEDGMENTS

I would like to first thank Professors Gang-yu Liu and Tonya Kuhl. They together taught me chemistry and chemical engineering, and the way to face science as a whole.

I am also grateful to the former and current Liu group members for sharing their knowledge with me: Yang Liu, Logan Swartz, Dr. James Kurniawan, Jiali Zhang, Dr. Jianli Zhao, Dr. Marshall van Zijll, Dr. Qingbo Yang, William Deng, Michael Tamsi, Victoria Tran, Dr. Shailise Ross, Shuo Wang, Dr. Arpad Karsai, Susan Stagner, Amanda Dang, and Daniel Kienle.

Many thanks to my third thesis committee member: Professor Atul Parikh.

Thanks also go to my collaborators: Jane Frommer (IBM Research Center, Almaden), and Pablo Dörig (Cytosurge, Switzerland).

Special thanks to Alan Hicklin, who helped me take my first steps using the atomic force microscope (AFM), scanning electron microscope (SEM), confocal fluorescence microscope, as well as during my first experiences with troubleshooting instruments.

Thanks to the Brazilian National Council for Scientific and Technological Development for the financial support of most of my PhD studies.

Finally, thanks to my parents, Rubens Paulo de Souza and Maria Isabel Ventrici de Souza. Without them, I would not be able to go through this journey.

Development of Advanced Methodologies for Three-Dimensional Nanoprinting

ABSTRACT

Three-dimension (3D) printers are commercially available with resolution as high as micrometers. Further miniaturization would require development of materials, instruments, as well as methodology, in order to attain required spatial precision to reach nanometer scale. This dissertation reports our recent progress in producing 3D nanostructures using atomic force microscopy (AFM) based methods. First, we use AFM to investigate and to better understanding of the tip-molecular and molecule-molecules interactions using bilayer systems to begin the studies. The structure, phase behavior and properties of cellular membranes are determined by their composition, which includes phospholipids, sphingolipids, sterols, and proteins with various levels of glycosylation. Due to the intricate nature of cellular membranes, a plethora of in vitro studies have been carried out with model membrane platforms that capture specific properties such as fluidity and permeability, but vastly simplify the membrane composition in order to focus in detail on a single property or function. Supported lipid bilayer (SLB) systems are one such platform and this work focuses specifically on the characterization and engineering of SLB systems. A number of characterization methods which take advantage of the flat orientation of SLBs are described and references which go into more depth are included. This dissertation reports quantity

and compares the quality of the resulting SLBs in correlation with a variety of gel and fluid compositions, preparation techniques and parameters, to generate general rules of thumb to guide preparation of designed SLB systems. Finally, our approaches to reduce morphologic defects are delineated.

Second, we use modified AFM technology for both printing and characterization. By putting molecules to the AFM tips, then transferring them to surfaces via scanning, nanometer scale lines, cross-grids, and pyramids were constructed following designed geometry and size. The products were also characterized in situ using AFM to demonstrate fidelity and spatial precision. Another approach taken in this dissertation towards the 3D nanoprinting goal is the direct delivery via combining AFM with microfluidic probes. Direct writing methods are a convenient way to produce 3D structures. The capability to extrude materials through a nozzle makes this method compatible with a wide range of inks. Although this method has been routinely used in the fabrication of structures on the microscale, the new challenge is to achieve 3D printing on the nanoscale. This dissertation reports the miniaturization of 3D structure production to line widths of 130 nm and heights of 3.1 nm. Three layered grids and custom designed objects were printed with the direct delivery of ultraviolet curable polymer using a modified atomic force microscope (AFM). The enabling aspects of 3D nanoprinting should have significant impact on a broad range of applications including tissue engineering, biomaterials, biomimetics, nanophotonics materials, and nanodevices.

TABLE OF CONTENTS

ACKNOWLEDGMENTS.....	iii
ABSTRACT	iv
LIST OF FIGURES.....	xi
LIST OF TABLES	xv
CHAPTER 1	1
INTRODUCTION.....	1
1.1. Scanning Probe Microscopy (SPM) as a lithographic tool	1
1.1.1. Motivation.....	1
1.1.2. AFM.....	1
1.1.3. FluidFM	2
1.2. Biomembrane models.....	2
1.2.1. Motivation.....	2
1.2.2. AFM as an analysis tool.....	3
1.3. Dissertation objective.....	3
1.4. Dissertation organization.....	4
CHAPTER 2	5
EXPERIMENTAL.....	5
2.1. AFM	5

2.1.1. Methodology.....	5
2.2. FluidFM microfluidic device	6
2.2.1. Conversion of image files into Cytosurge vector files	6
2.3. SEM.....	9
2.3.1. Sample preparation	9
2.3.2. Methodology.....	9
2.4. Substrate preparation.....	10
2.4.1. Glass and Silicon	10
2.4.2. Mica (0001) surfaces	10
CHAPTER 3.....	11
PREPARATION AND CHARACTERIZATION OF SOLID SUPPORTED LIPID BILAYERS – CONSTRUCTING AN EFFECTIVE BIOMEMIMETIC MEMBRANE....	11
3.1. Introduction	11
3.2. Primary Methods in Preparation of Solid Supported Bilayers.....	13
3.2.1. Langmuir-Blodgett (LB) Technique.....	13
3.2.2. Langmuir-Schaefer (LS) Technique.....	17
3.2.3. Vesicle Fusion (VF) Technique.....	18
3.2.4. Spreading and Spin Coating Techniques.....	20
3.3. Characterization of Solid Supported Bilayers.....	20
3.3.1. Atomic Force Microscopy (AFM).....	21

3.4.	Exploration of Ideal SLB Deposition Conditions	23
3.4.1.	Quantification of SLB quality by transfer ratio experiments.....	24
3.4.2.	Surface chemistry and substrate roughness.	24
3.4.3.	Lipid phase state.	25
3.4.4.	Effect of drying the inner monolayer.....	25
3.4.5.	AFM Characterization of Membrane Defects to assess SLB Quality	27
3.4.6.	Lipid phase state and substrate roughness on the quality of inner monolayer.....	27
3.4.7.	Significance of interleaflet coupling and packing of inner monolayer on SLB quality 29	
3.4.8.	Preparation technique and quality of SLBs	31
3.4.9.	Cholesterol in altering the phase state and SLB quality	32
3.4.10.	Surface pressure/area per molecule.....	33
3.5.	Conclusion.....	35
3.6.	Acknowledgements	36
CHAPTER 4	37
DEVELOPMENT OF A NEW METHODOLOGY FOR BUILDING THREE-DIMENSIONAL NANOSTRUCUTRES	37
4.1.	Introduction	37
4.2.	Materials and Methods.....	38
4.2.1.	Materials.....	38

4.2.2.	Preparation of substrate.....	38
4.2.3.	AFM.....	38
4.3.	Results	39
4.3.1.	3D printing of line arrays.....	39
4.3.2.	3D nanoprinting retains the fidelity of the design	40
4.3.3.	3D printing of stacked grids	40
4.4.	Conclusion.....	41
4.5.	Acknowledgements	42
CHAPTER 5	43
THREE-DIMENSIONAL NANOPRINTING USING DIRECT DELIVERY	43
5.1.	Introduction	43
5.2.	Experimental	44
5.2.1.	Materials	44
5.2.2.	Scanning electron microscopy Imaging.....	44
5.2.3.	Atomic force microscopy imaging.....	45
5.3.	Results and Discussion.....	45
5.3.1.	AFM-based nanofluidic device for delivery.....	45
5.3.2.	3D nanoprinting of stacked grids.....	46
5.3.3.	3D nanoprinting of complex structures by design.....	50
5.4.	Conclusion.....	53

5.5. Acknowledgements	53
CHAPTER 6	54
ON-GOING AND FUTURE WORK	54
6.1. Three-Dimensional display of AFM stacked layers of images	54
APPENDIX	60
A.1. Standard Operation Procedures	60
A.1.1. Cytosurge FluidFM.....	60
A.1.1.1. Experiment preparation steps	60
A.1.1.2. Spotting	62
A.1.1.3. Spotting Calibration SOP	66
REFERENCES.....	68

LIST OF FIGURES

- Figure 2-1. ImageJ software treatment of a .jpg image. In this image is possible to see the yellow contour of the traces of the object. The yellow outline will be used by the software to determine its XY coordinates..... 6
- Figure 2-2. XY coordinates of an object shown in a notepad file. 7
- Figure 2-3. XY coordinates of an object shown in an excel file. The first row also displays the values to be used as speed and pressure in columns C and D, respectively. 8
- Figure 2-4. A notepad file showing XY coordinates together with speed and pressure values, separated by commas. This file is ready to be read by the FluidFM. 9
- Figure 3-1. [A] Schematic of the process of LB deposition of solid supported bilayers. (Left) After immersing the substrate, lipid is deposited on the air-water interface and compressed to the desired surface pressure. (Center) The substrate is drawn out of the subphase through the interface to deposit the inner leaflet. (Right) After the inner monolayer deposition is done, the substrate is then lowered through the interface to deposit the outer leaflet layer. [B] Langmuir-Schaefer (LS) method to deposit the outer leaflet on an LB deposited inner monolayer leaflet. [C] Vesicle fusion on an LB deposited monolayer. [D] Vesicle fusion directly onto a clean hydrophilic substrate. [E] Top three are AFM topograph, 20 μm x 20 μm of an 1:1:1 DPPC-DOPC-cholesterol deposited via LB, LS, and VF, respectively. The support is a 1,2-dipalmitoyl-*sn*-glycero-3-phosphoethanolamine (DPPE) LB monolayer formed at surface pressure of 45 mN/m and dipping speed of 1 mm/min. The LB and LS of the outer layer were done at pressure of 30 mN/m. The bottom images show the comparison of the SLB quality deposited as asymmetric vs symmetric bilayer on a glass substrate using vesicle fusion (VF) visualized using fluorescence microscopy (FM). 16
- Figure 3-2. 45 μm x 45 μm AFM image of a 3:7 DPPE-DOPC SLB on DPPE covered mica (0001), revealing a gel-phase DPPE domain. The SLB was asymmetric because of the difference between inner DPPE monolayer and outer 3:7 DPPE-DOPC monolayer. Scale bar = 10 μm 23
- Figure 3-3. Representative 10 μm x 10 μm AFM topography scans of various monolayers LB deposited with dipping speed of 1 mm/min on mica. The DPPE and DPPC monolayer were

deposited at surface pressure of 45 mN/m and the 92:8 DPPC-chol. and 80:20 DPPC-chol. were deposited at surface pressure of 30 mN/m.	28
Figure 3-4. Representative 10 μm x10 μm AFM topography scans of DPPC monolayers LB deposited at surface pressure of 45 mN/m on mica (A), silicon wafer (B), and glass slide (C).	29
Figure 3-5. Representative 10 μm x10 μm AFM topography scans of DPPC and 92:8 DPPC-chol. deposited as symmetric or asymmetric (on DPPE monolayer) bilayer showing varying amount of membrane imperfections. Defects only span the outer monolayer while holes span the membrane to the underlying support. The number of defects and holes in the table was based on 2-4 samples with at least 5 scans per sample yielding 10-20 analyzed images.	30
Figure 3-6. 10 μm x 10 μm AFM topography images showing defect density as function of cholesterol concentration in a DPPC outer leaflet at 25 $^{\circ}\text{C}$. The outer monolayers were deposited on a near defect-free DPPE inner monolayer on mica.	33
Figure 3-7. Effect of surface pressure on defects in LB deposited 92:8 DPPC-cholesterol on DPPE. Insets are 10 μm x 10 μm AFM topograph at surface pressure of 20, 30, and 40 mN/m, respectively. The outer leaflet was deposited at dipping speed of 1 mm/min and 25 $^{\circ}\text{C}$	35
Figure 4-1. A 5x5 μm AFM topographic image revealing 6 lines printed on a Si(111) wafer surface. The lines were composed of different numbers of passes of the AFM tip. From the left to the right: 40, 30, 20, 10, 4 and 2 passes. The height of those lines varied in accordance with the number of passes. From the left to the right the heights were: 4.1, 2.7, 1.9, 1.7, 1.1 and 0.5 nanometers.	39
Figure 4-2. A 5x5 μm AFM topographic image revealing 6 lines printed on a Si(111) wafer surface. The lines were each produced by 20 passes. Cursor profiles allow measurements of line height and width at the defined locations.	40
Figure 4-3. A 10x10 μm AFM topographic image revealing 6 lines printed on a Si(111) wafer surface.	41
Figure 5.1. [A] Schematic diagram of the key parts of the combined AFM and microfluidics for 3D nanoprinting. [B] SEM image of the microfluidic AFM cantilever used in this work. [C] A zoom-in view of the tip apex showing the size of the opening atop.	46

Figure 5-2. Schematic diagram of the printed grids. [A] The first layer (grey) is the base of the stack with overall dimensions of 1mm x 1mm. [B] The second layer (black) lies on top of the first layer and is oriented perpendicular to the first set of lines. [C] The third layer (red) lies on top of the second layer and is perpendicularly oriented with respect to the second layer; hence, it has the same orientation as the first layer. [D] Zoom-in of the grid showing the 20 μm periodicity of the lines 47

Figure 5-3. [A] A 1.1 mm x 1.4 mm SEM image showing the 3-layered printed grid. [B] a 40 μm x 40 μm AFM topographic image to reveal the detail of the grid region of the red box of (A). [C] 3D rendition of the AFM topography image of (B). [D] 2 cursor profiles as indicated in (B): the red cursor crosses the superimposed 1st and 3rd layer of the grids, and the black cursor crosses 2 lines in the 2nd layer of grids. The left peaks are superposed ($\Delta x = 0$), so the precision in the superposition of the peaks in the right can be determined. [E] A zoom-in view of the right peak in (D). The center of the grids is aligned with 4.8 nm precision. 48

Figure 5-4. Schematic diagram of the process of printing a 3-layer four-leaf clover: layer one shown in black, layer two in gray, and layer three in red. 51

Figure 5-5. [A] SEM image of clovers 1-6 made of Loctite® AA 349™ on a glass slide substrate. [B] 3D display of an AFM topographic image of clover 6 as indicated in the red frame in (A). [C] 3D display of an AFM topographic image of the smallest 3D structure, clover 7. 52

Figure 6-1. Illustration of the issue with multi-layered structures and the absence of inner features information under AFM conventional display methods. 54

Figure 6-2. Three layered structure imaged in between deposition steps. The first row shows the AFM topographic images of the structures at 3 different steps, while the second row shows the corresponding images after being processed by the macro. 55

Figure 6-3. Resulting 3D display of the 3 overlapped images, representing the 3 layers of material in this structure. Each layer is represented with a different color in the figure. 56

Figure 6-4. AFM topographic images of a three-layered square “pyramid”. The first layer has the largest square as the base and the following squares are systematically smaller and inserted into the base. 57

Figure 6-5. AFM topographic images of a three-layered square “pyramid”. The first layer has the smallest square as the base and the following squares are systematically larger and built on top of the base. 58

LIST OF TABLES

Table 3-1. Transfer Ratio Summary of Various Lipid Mixtures deposited with the LB technique.	26
Table 5-1. Lateral dimensions of seven clovers printed in the scheme of Figure 4-4. For all clovers, the ratio of dimensions is constant, $a/b = 1.15$	51

CHAPTER 1

INTRODUCTION

1.1. Scanning Probe Microscopy (SPM) as a Lithographic Tool

1.1.1. Motivation

New methods for building hierarchical structures, crossing several orders of magnitude within the same object, are the focus of research in many different areas, including lightweight structures, semiconductors, batteries, and photonics. The variety of materials, length scales, and architectures are the driving force of research in this area. Three-dimensional (3D) printing is the process of fabrication of structures in a layer by layer fashion and it can be achieved using different methods, such as direct writing, or laser-writing optics, to fabricate materials layer by layer.

The use of SPM technique to achieve the delivery of various materials to a surface with nanometer accuracy has been reported in the literature.¹⁻² The ability of producing features with this level of precision is due to the positioning by piezo mechanics and nanometer sharp probes. Such high precision positioning instrumentation enables the fabrication of nanostructures onto a surface. The high accuracy in the repeatability of the positioning of the probe enables the delivery layers on top of the previously delivered ones, which makes 3D possible.³⁻⁴

1.1.2. AFM

In an AFM instrument, a sharp tip is raster-scanned over a surface using a feedback loop to adjust parameters needed to image a surface. The interactions between the tip and the sample result in a map of the resulting atomic forces. With the help of graphics processing tools, an image is then produced. Piezo materials are used in the movement controller systems of the device. Such materials are capable of yielding a precision in the order of angstroms. The z displacement of the probes, while the scan is being performed, is detected by the deflection of the probe holding the sharp tip. Traditionally,

most AFMs use a laser beam reflected from the back of the probe and onto a 4 quadrants photodiode detector. AFM tips and cantilevers are typically made of Si or Si₃N₄. Typical tip radius is from a few nanometers to tens of nanometers. AFM has a feedback loop system that controls the tip position and the force by using the information generated by the deflection of the cantilever.

1.1.3. FluidFM

The FluidFM instrumentation is a combination of the high precision machinery of the SPM instruments with convenience of the microfluidics extrusion devices. This instrument, just like the AFM, is composed of a high precision positioning system, a probe with a sharp tip and a laser reflecting onto a photodiode detector. However, in this method, the probe is microchannelled and connected to a pressure control system. The combination of all of these features results in a lateral positioning precision of 10 nm in a 240 x 74 mm range, a z-movement precision of 4 nm in a 50 mm range, and a pressure precision of 1 mbar in a -800 to 1000 mbar range. The probes are produced in various shapes and configuration. Tip apertures range from 300 nm to 8 μm with elasticity constant of 0.2 N/m and 2.0 N/m.

1.2. Biomembrane Models

1.2.1. Motivation

The complexity of cellular membranes, due in large part to the enormous variety of chemical species present and their active functions, makes their study challenging. In addition, cellular membranes are constantly in flux and dynamically respond to their local environment. Together, these properties make it daunting to tease out temporal and spatial variations and even more difficult to correlate structure-function relationships. To make headway, various biomimetic or model membrane platforms have been developed. Though vastly simplified, these model membranes can still mimic the essential physical and chemical properties of biological membranes such as membrane elasticity, fluidity, and phase behavior, and can provide an appropriate environment for studying protein function.⁵ Recently,

biomimetic membranes which recapitulate the various phases that are thought to co-exist in biological membranes such as liquid-order (L_o), liquid-disordered (L_d), and gel phases are being actively studied. Solid supported biomimetic bilayers immobilized on clean smooth surfaces have emerged as a powerful platform to study biomimetic membranes, including lipid rafts and small-molecules such as polypeptides and membrane proteins on the nanoscale.

1.2.2. AFM as an Analysis Tool

Atomic force microscopy provides a powerful means to characterize solid supported bilayer systems due to its high-resolution, label-free nature and versatility to work in various environments, including ambient, liquid and culture media.⁶⁻⁷ Local structure and property have been clearly revealed by AFM including topography, domain size, layer thickness, friction, adhesion, and visco-elastic properties.⁸⁻¹¹

1.3. Dissertation Objective

The primary goal of this dissertation research is to develop and report new methodologies for the production of 3D nanostructures by means of delivery in a layer by layer fashion. Such a process is typically known as 3D nanoprinting. Manipulating various materials used as “ink” in the process and utilizing various techniques to achieve this primary goal is within the interests of this dissertation. Once 3D nanoprinting is achieved, the focus changes to the production of custom designed hierarchical structures. Finally, the second goal of this dissertation is to demonstrate the ability of the AFM in the analysis of supported lipid bilayers (SLBs) with a resolution that traditional techniques, such as fluorescence microscopy, cannot achieve. An analysis of the quality of the produced SLBs is also illustrated.

1.4. Dissertation Organization

Following this introductory chapter, Chapter 2 describes the experimental methods and techniques utilized in this dissertation work, such as SEM, AFM, FluidFM and substrate preparation. Chapter 3 describes the fabrication and characterization of 3D nanostructures through direct delivery of ink using an AFM in contact mode. Chapter 4 describes the fabrication and characterization of 3D custom designed hierarchical structures through direct delivery of ink using a nanofluidic AFM device. Chapter 5 reports the analysis of SLBs using AFM and shows a comparative study with various SLB fabrication techniques and the resulting local surface structure quality. Finally, Chapter 6 provides insight to the future directions of the work reported in this dissertation.

CHAPTER 2

EXPERIMENTAL

2.1. AFM

2.1.1. Methodology

Since its invention in 1986, AFM has become a powerful tool for the characterization of materials and surfaces due to its high spatial resolution. Typical lateral and vertical resolutions of AFM for a crystal surface can reach as high as 0.1 and 0.01 Å, respectively. The most common and widely used AFM imaging mode is contact mode, or constant force mode. This mode is associated with the interatomic repulsion between probe and substrate, known as van der Waals force. In addition to the van der Waals force, two other forces are generally present in contact mode: capillary force from a thin layer of water often presents in ambient conditions; and the force exerted by the cantilever itself. In contact mode imaging, the tip deflection is maintained constant. The z output voltage signal from feedback system is used to produce the topographic image. Tapping mode is the second most used mode in AFM. In this mode, the AFM tip is fixed to a piezo and an oscillating voltage is applied at near the resonance frequency of the cantilever. The probe oscillates at a certain amplitude which decreases when the tip touches the surface. A feedback system will adjust the movement of the piezo up or down in order to keep the amplitude constant. The output z voltage is used to generate the topographic image of the surface. Both contact and tapping mode were used in this work and the specifics are described in the experimental sections of each chapter. A MFP-3D-Bio AFM (Oxford Instruments, Santa Barbara, CA, USA) was used to perform the delivery of the polymer to the substrates. An AC240 (Olympus America, Central Valley, PA, USA) cantilever with a 1.7 N/m spring constant and 57 kHz resonant frequency was chosen to scan

all samples. Images were processed using Gwyddion open source software, which is freely available on the Internet and supported by the Czech Metrology Institute.

2.2. FluidFM Microfluidic Device

2.2.1. Conversion of Image Files into Cytosurge Vector Files

- Open the image with ImageJ. The image must be black and white.
- Click anywhere in your image so you can select it. A yellow outline will appear on the contour of your figure.

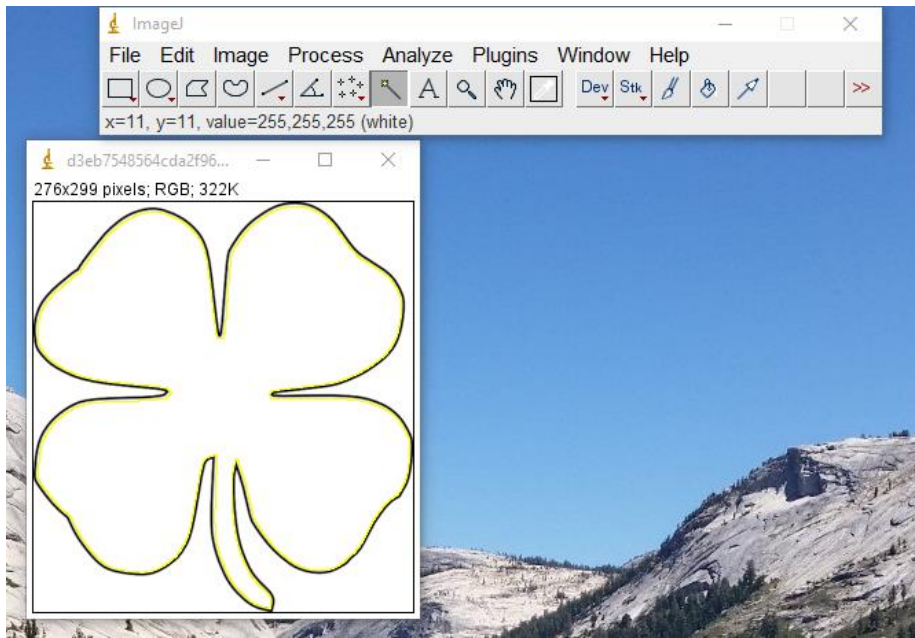


Figure 2-1. ImageJ software treatment of a .jpg image. In this image it is possible to see the yellow contour of the traces of the object. The yellow outline will be used by the software to determine its XY coordinates.

- Click File -> Save as -> XY coordinates. That will generate a .txt file with two non-separated columns.

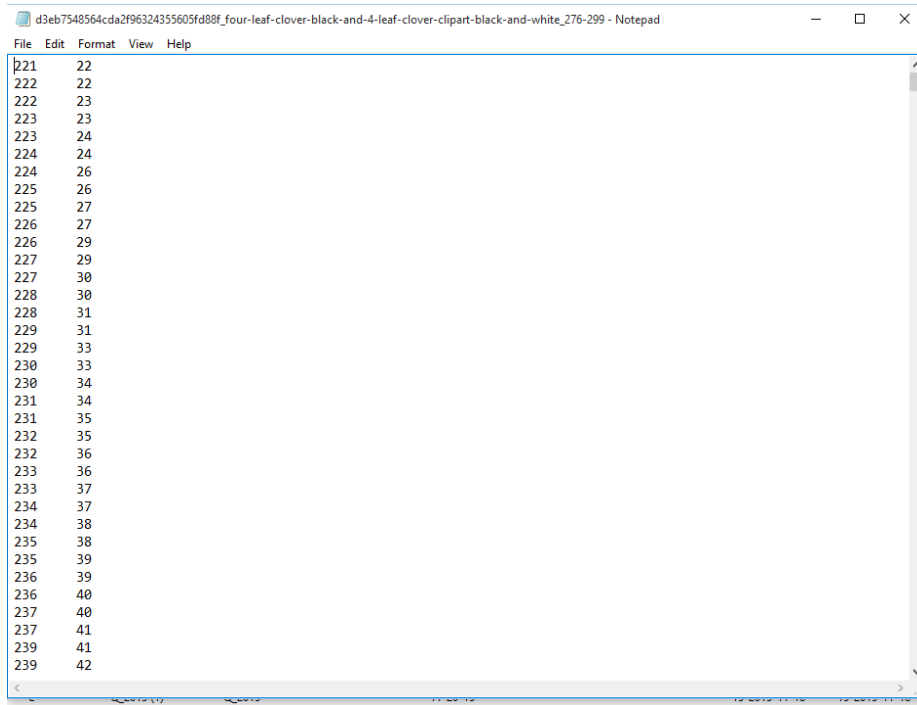


Figure 2-2. XY coordinates of an object shown in a notepad file.

- Copy all the data.
- Open Excel and select two entire columns. Paste your copied data in there. A pop-up window may show up saying “The data you’re pasting isn’t the same size as your selection. Do you want to paste anyway?”. Click Ok.
- Type the values for the intended pressure in C1 and for the intended speed in D1.

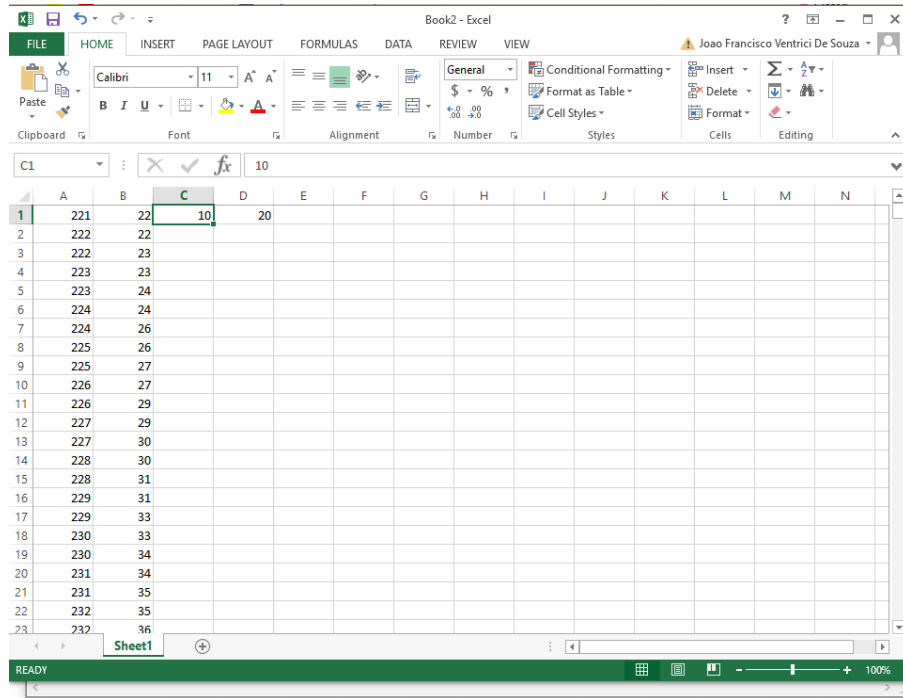


Figure 2-3. XY coordinates of an object shown in an excel file. The first row also displays the values to be used as speed and pressure in columns C and D, respectively.

- Drag the corner of each of those cells until the last populated row.
- Click File-> Save as. Locate the folder you intend to save the file. Under the “Save as type” box, select CSV (comma delimited).
- Open your file with Notepad to check the outcome.

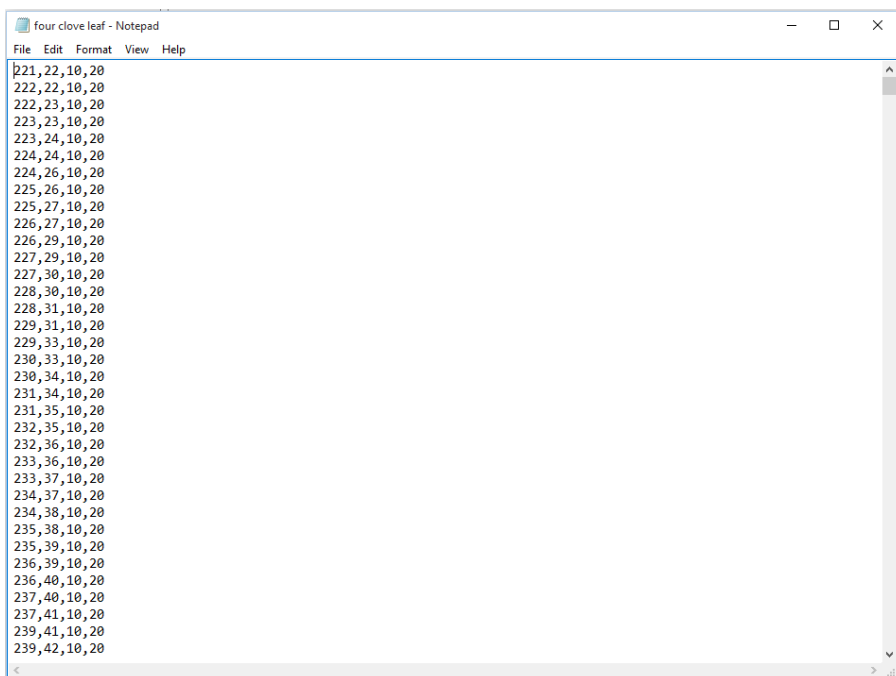


Figure 2-4. A notepad file showing XY coordinates together with speed and pressure values, separated by commas. This file is ready to be read by the FluidFM.

- If your file has four columns separated by commas, you are done! Just load the file to Arya and print your structure.

2.3. SEM

2.3.1. Sample Preparation

To avoid charging, a thin layer (4 nm) of gold (Alfa Aesar, 99.999%) was evaporated onto the glass slide, coating the printed structures, using a high-vacuum evaporator (DV502-A, Denton Vacuum, Moorestown, NJ, U.S.A.), at a base pressure below 2×10^{-6} Torr and evaporation rate of 1.5 \AA/s .

2.3.2. Methodology

SEM images were acquired on a Hitachi S-4100T FE-SEM (Hitachi High Technologies America, Inc., Pleasanton, CA, USA), using an accelerating voltage of 2 kV at 10 \mu A .

2.4. Substrate Preparation

2.4.1. Glass and Silicon

The 1" x 3" glass slides and silicon wafers were cleaned by immersion in Piranha solution, which consists of 3 parts of sulfuric acid to 1 part of hydrogen peroxide 30%, for 2 hours. The clean glass slides and silicon pieces were rinsed with MilliQ water and dried under a constant flow of nitrogen for 5 minutes. Substrates were prepared and used the same day to guarantee a clean surface at the nanoscale.

2.4.2. Mica (0001) Surfaces

Mica (S&J Trading Company, New York, clear ruby muscovite) was cut into 1 cm x 1 cm pieces and freshly cleaved right before lipid deposition to ensure cleanliness of the surface. No further pretreatment was done before lipid deposition.

CHAPTER 3

PREPARATION AND CHARACTERIZATION OF SOLID SUPPORTED LIPID BILAYERS – CONSTRUCTING AN EFFECTIVE BIOMEMIMETIC MEMBRANE

3.1. Introduction

The human body consists of billions of cells, the smallest building block of life. Cells themselves, their organelles, and other functional volumes are compartmentalized by membranes that encapsulate various essential biomolecules such as nucleic acid and proteins which regulate cellular function.¹² The membranes themselves contain hundreds of different constituent molecules, including lipids, sterols, and proteins. These moieties interact laterally to create lipid rafts where the majority of cellular signaling and transport is thought to take place.¹³⁻¹⁵ One of the earliest studies to fundamentally determine the structure of a cell membrane was performed by Gortner and Grendel in 1925.¹⁶ Using a Langmuir trough, they determined that the membrane of mammalian red blood cells was formed by two lipid monolayers. Langmuir troughs are still used extensively today to precisely measure the properties of lipid monolayers as well as to deposit monolayers to form well-defined model membrane systems.

The complexity of cellular membranes, due in large part to the enormous variety of chemical species present and their active function, makes their study challenging. In addition, cellular membranes are constantly in flux and dynamically respond to their local environment. Together, these properties make it daunting to tease out the temporal and spatial variation and even more difficult to correlate structure-function relationships. To make headway, various biomimetic or model membrane platforms have been developed. Though vastly simplified, these model membranes can still mimic the essential physical and chemical properties of biological membranes such as membrane elasticity, fluidity, phase behavior, and can provide an appropriate environment for studying protein function.⁵ Recently, biomimetic membranes which recapitulate the various phases that are thought to co-exist in biological

membranes such as liquid-order (L_o), liquid-disordered (L_d), and gel phases are being actively studied. For example, membranes containing mixtures of saturated lipid with high melting point, unsaturated lipid with low melting point, and sterols can form a variety of coexisting phases and partitioning of different molecules into these phases has been of particular interest.

In an earlier review, Castellana and Cremer¹⁷ described a number of lipid bilayer platforms that have been used as model membrane systems. These platforms allow studying a variety of processes. For example, free standing black lipid membranes are used to study transport across membrane, while phase behavior and membrane fluidity are frequently studied using giant unilamellar vesicles. Solid supported lipid bilayers (SLBs) are used to quantify membrane topography and adhesion. Some of the model membrane platforms provide overlapping information, but the specific type of platform dictates the characterization techniques that can be used. Powerful surface sensitive techniques for probing adhesion and high-resolution scans of membrane topography can only be performed using solid supported membrane platforms. Free-standing membrane platforms such as unilamellar or multilammellar lipid vesicles enable studies free from the influence of the underlying inorganic support and are useful systems for micropipette mechanical measurements, small angle scattering, and various imaging microscopy, but are incompatible with most high resolution, nanoscopic characterization techniques. As a result, solid supported biomimetic bilayers immobilized on clean smooth surfaces have emerged as a powerful platform to study biomimetic membranes, including lipid rafts and small-molecules such as polypeptides and membrane proteins on the nanoscale. However, studies of integral membrane proteins (IMPs) using SLB platforms are limited due to the potential interaction of the protein with the underlying support¹⁸⁻²⁰, which can lead to the denaturation of the embedded proteins. SLBs can be modified with polymeric spacers and tethers to increase the separation between the membrane and support. Such platforms are typically referred to as polymer cushioned and are becoming more widely utilized.²¹⁻²⁶

This instructional review focuses on solid-supported bilayer systems and is organized into three main sections. In the first, different methods to prepare SLBs are described in detail while the second part of the review covers commonly used characterization techniques of supported membrane systems. The last section of the paper discusses preparation techniques that can be used to create almost defectless SLBs with supporting data from various characterization techniques.

3.2. Primary Methods in Preparation of Solid Supported Bilayers

There are two main methods used to create solid supported bilayers: Langmuir trough deposition technique and vesicle fusion. These methods can be used separately or in conjunction to create symmetric and asymmetric membranes. More recently solvent spreading and spin coating have emerged as additional, rapid means to fabricate solid supported membranes. Details for each deposition technique are provided below.

3.2.1. Langmuir-Blodgett (LB) Technique.

The LB technique, which dates back to 1917, was pioneered by Irving Langmuir²⁷ for depositing fatty acid monolayers from the air-water interface onto solid substrates. Katherine Blodgett²⁸ then used the same technique to deposit multilayers of fatty acids with repeated dipping of the solid substrate through the air-water interface. The technique has subsequently been used to deposit monolayers of lipids and other surface active, water insoluble films onto substrates. The trough, usually made with a low surface energy material such as Teflon, is filled with water or any other subphase such as physiological buffer solution. Widely used substrates include mica²⁹⁻³⁰, quartz³¹⁻³², borosilicate glass (microscope slides)^{31, 33}, silicon wafers, and thin films of metal³⁴⁻³⁵ or silicon dioxide (SiO₂)³⁶. The quality of the transfer is greatly enhanced by using ultra-clean, hydrophilic substrates with low surface roughness resulting in better packed, uniform SLBs. Most high-resolution studies use mica or high

quality oxidized silicon wafers because of their low root mean square roughness, 0.2 Å and 2-3 Å, respectively. To ensure substrate cleanliness, mica should be freshly cleaved right before use. We typically prepare our quartz and silicon wafer substrates through methodical cleaning steps: sonicated in acetone, transferred and sonicated in isopropanol and then rinsed in copious MilliQ water to remove contaminants. We then sonicate the substrate in Hellmanex (Hellma Analytics) soap and again rinse with copious MilliQ water. The substrate is then dried using clean nitrogen gas. The cleaned and dried substrate is subsequently treated for at least 30 minutes with plasma-ozone and used immediately after the UV-ozone treatment. Hydrophilic substrates are immersed in the subphase before deposition of lipids on the air-water interface. For atomic force microscopy (AFM) measurements, mica is typically used because it can be easily cleaved to be atomically smooth over relatively large areas. The lipid spreading solution is prepared in a solvent, such as pure chloroform or a mixture of chloroform:methanol. The concentration of the spreading solution is typically between 0.1 to 1 mg/mL. The lipid must fully dissolve in the solvent, and solvent solubility in the trough subphase should be minimal. The choice of solvent and concentration is determined by the solubility of the lipids in the chosen solvent. For example, phosphatidylcholine (PC) lipids are fully dissolved in chloroform at room temperature, but phosphatidylethanolamine (PE) lipids require a mixture of 9:1 chloroform:methanol for complete dissolution.

The spreading solution is dispensed carefully onto the air-water interface, droplet by droplet, to create a thin layer of lipids whose hydrocarbon tails face away from the water subphase. An arbitrary solution concentration is chosen to achieve a recommendable volume of 50 to 100 μL , depending on the surface area of the LB trough and desired compression of the film. Once the solvent has evaporated, a barrier compresses the lipid monolayer to create a highly compressed two-dimensional film on the air-water interface at a pre-determined surface pressure. After reaching the target pressure and allowing the

compressed film to equilibrate, the solid hydrophilic substrate is vertically drawn out of the water to deposit the inner monolayer. Throughout the deposition process, the surface pressure is usually kept constant by compressing the remaining film as the transfer occurs. Once the substrate has cleared the water level, it is resubmerged to deposit the outer monolayer of the SLB. This process, known as LB/LB deposition, can deposit a bilayer featuring a single component lipid or mixtures of lipids with few defects. The composition of the bilayer leaflets may be identical or different for the inner and outer monolayer (symmetric vs. asymmetric/hybrid bilayer). A diagram for bilayer deposition through LB/LB technique is shown in Figure 3-1[A].

Some important parameters must be considered in order to achieve a high-quality solid supported membrane through the LB deposition technique. During deposition, the phase of the lipids greatly affects the resulting monolayer transfer onto the substrate. Lipid phase is dictated by lipid type, subphase temperature, and the film's surface pressure (as measured by a Wilhelmy plate). Optimum deposition pressures are usually assessed through surface pressure vs. area per lipid molecule plots, Π -A isotherms of the lipid or mixture being deposited. In general, high changes in surface pressure per area, $\frac{d\Pi}{dA}$, correspond to better transfers to the substrate. The transfer ratio, $TR = \frac{\Delta A_{trough}}{A_{substrate}}$, is used to quantify the quality of the transfer of material from the air-water interface where a $TR = 1$ indicates that area per molecule and surface pressure are maintained from the air-water interface to the substrate.³⁷⁻³⁸ Dipping speed must also be considered in order to achieve an efficient transfer of lipid from the air-water interface to the solid substrate. A relatively high transfer ratio cannot be obtained if the substrate moves too quickly through the lipid monolayer. In addition, a fast dipping speed sometimes causes delamination of the inner monolayer rather than deposition of the outer layer. Typically, a dipping speed between 1 to 4 mm/min is chosen in order to obtain a high transfer ratio ($TR \sim 1.0$). Details for parameters required to

obtain an SLB with as few defects as possible are discussed in section 4 and an in-depth discussion of the LB technique can be found in the following reference.³⁹

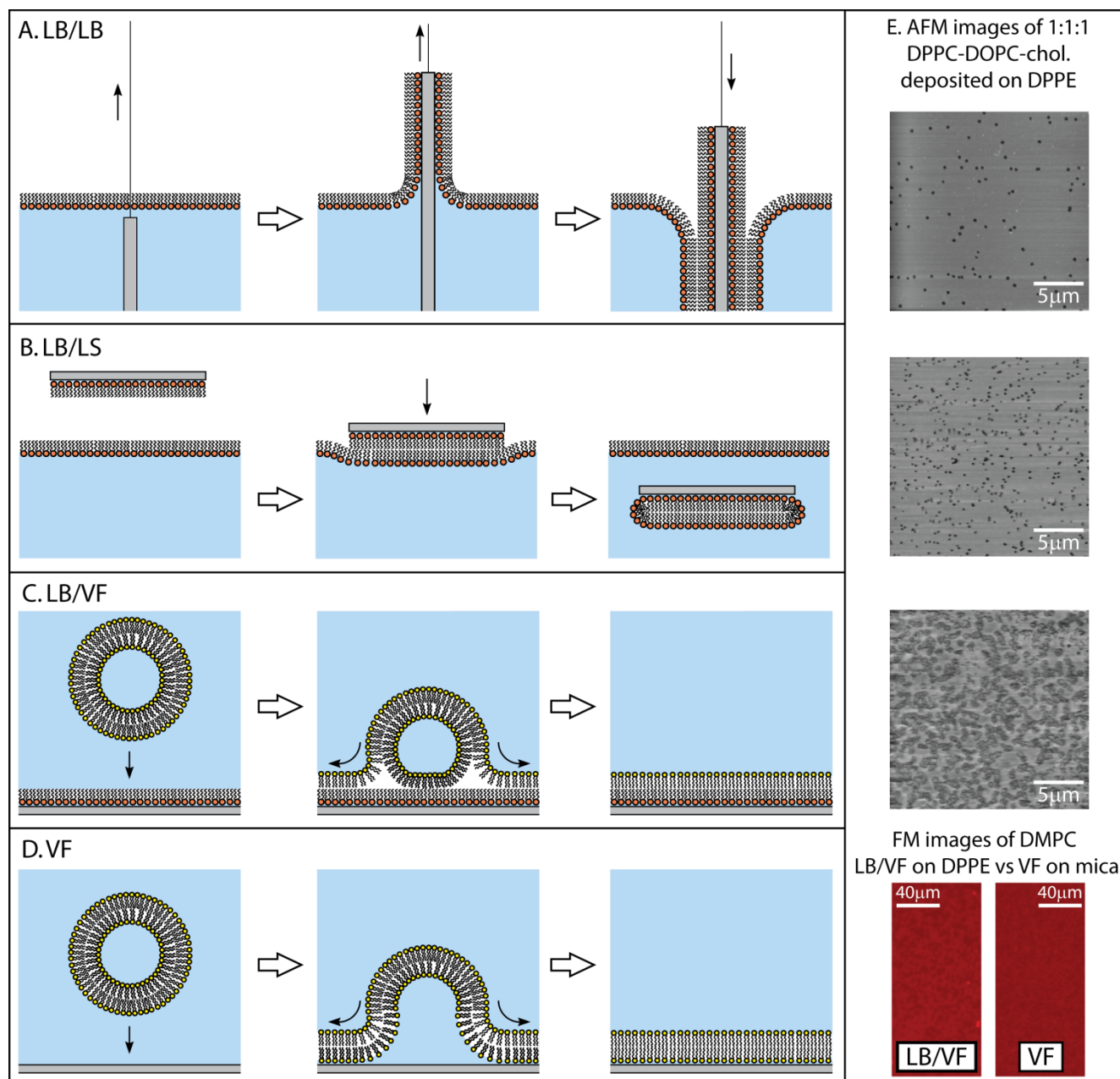


Figure 3-1. [A] Schematic of the process of LB deposition of solid supported bilayers. (Left) After immersing the substrate, lipid is deposited on the air-water interface and compressed to the desired surface pressure. (Center) The substrate is drawn out of the subphase through the interface to deposit the inner leaflet. (Right) After the inner monolayer deposition is done, the substrate is then lowered through the interface to deposit the outer leaflet layer. [B] Langmuir-

Schaefer (LS) method to deposit the outer leaflet on an LB deposited inner monolayer leaflet. [C] Vesicle fusion on an LB deposited monolayer. [D] Vesicle fusion directly onto a clean hydrophilic substrate. [E] Top three are AFM topograph, 20 μm x 20 μm of an 1:1:1 DPPC-DOPC-cholesterol deposited via LB, LS, and VF, respectively. The support is a 1,2-dipalmitoyl-*sn*-glycero-3-phosphoethanolamine (DPPE) LB monolayer formed at surface pressure of 45 mN/m and dipping speed of 1 mm/min. The LB and LS of the outer layer were done at pressure of 30 mN/m. The bottom images show the comparison of the SLB quality deposited as asymmetric vs symmetric bilayer on a glass substrate using vesicle fusion (VF) visualized using fluorescence microscopy (FM).

3.2.2. Langmuir-Schaefer (LS) Technique.

Vincent Schaefer, in collaboration with Irving Langmuir, first deposited a monolayer of urease on metal and glass plates with a method similar to the LB technique.⁴⁰ The LS technique, sometimes called horizontal deposition, deposits a lipid monolayer by dipping the substrate with a parallel orientation to the air-water interface through a compressed lipid monolayer (Figure 3-1[B]). Typically, the LS technique is used to deposit the outer leaflet of the membrane to create symmetric or asymmetric SLB with the inner monolayer deposited by LB. LS is particularly useful for SLB formation on glass where the inner monolayer can delaminate from the substrate during vertical LB deposition.⁴¹ In cases where the physiochemical interaction of the inner layer is insufficient to ensure the stability, the LS technique should be used to create the SLB.

Similar to the LB deposition method, lipid phase state is also important for the LS technique. In works involving asymmetric SLBs, which are typically used for study of lipid flip-flop rate⁴²⁻⁴⁴, gel phase lipids should be used as deposition of fluid phase lipids induced mixing between the inner and outer leaflet due to mechanical shock from LS method as demonstrated by Gerelli *et al.*⁴⁵ Dipping speed is not as crucial for achieving a quality bilayer. However, the orientation (that is, how level the substrate surface is relative to the water surface) is critical for successful LS deposition. When the substrate is at

an angle, film material can be pushed away leading to a less well-packed transfer. A detailed comparison of the SLBs fabricated with LB-LS technique versus LB-LB technique is provided in section 4.

3.2.3. Vesicle Fusion (VF) Technique.

The majority of SLB studies use the vesicle fusion method to prepare bilayers on solid substrates because of the ease and simplicity of this approach. To create an SLB, vesicles are incubated either on a monolayer of lipids deposited through LB technique to create an asymmetric bilayer (Figure 3-1[C])⁴⁶ or a clean hydrophilic surface to create a symmetric bilayer (Figure 3-1[D]). However, the quality of the asymmetric SLB deposited using LB/VF technique is lower compared to LB/LB or LB/LS deposited asymmetric bilayer (Figure 3-1[E]). In Langmuir trough techniques, the surface pressure of the monolayer is precisely controlled which generally leads to few defects and variation in the SLB. Vesicle fusion relies on the instability of vesicles interacting with the support (and frequently instability of the vesicles themselves in the solution) and attractive interactions of the vesicles with the support to yield spontaneous SLB formation. Osmotic stress, addition of divalent ions, and temperature cycling can also be done to aid SLB formation.⁴⁷⁻⁴⁹ Similarly, the quality of the symmetric bilayer formed by vesicle fusion to a hydrophilic substrate is also lower in quality.³² In one of the few direct comparison of LB deposited and vesicle fusion SLBs, Watkins *et al.*³⁷ established that 1,2-dipalmitoyl-*sn*-glycero-3-phosphocholine (DPPC) membranes deposited by vesicle fusion mimic depositions by LB technique at surface pressures of 38 ± 3 mN/m.

The first step in performing vesicle fusion is preparation of the vesicle solution. A small amount of concentrated lipid solution in organic solvent (~100 μ L of 10 mg/mL lipid solution in chloroform or a chloroform:methanol mixture) is prepared in a vial or similar container. The solvent is then evaporated by a stream of nitrogen to leave a thin lipid layer on the wall of the container. The amount of the lipid solution needed depends on the required volume of the vesicle solution. In general, the concentration of

a vesicle solution used for SLB formation is between 0.2 to 1 mg/mL. After drying with nitrogen, the lipids are placed in a vacuum for at least 4 hours to fully remove all solvent before hydrating the lipids to create the vesicle solution. Applying a vacuum is essential as any solvent present upon addition of water will disturb the formation of vesicles. After drying, the lipids are hydrated with water or a salt buffer solution and vortexed to obtain multilamellar vesicles of heterogeneous sizes. Small unilamellar vesicles (SUVs) are preferable for vesicle fusion because they are more readily absorbed onto a substrate to form a single SLB. To make the small vesicles, the vortexed vesicles are probe-tip sonicated or extruded through a polycarbonate membrane to create SUVs of a small, homogeneous size distribution. Extrusion is the preferred method, as probe-tip sonication can release contaminant titanium particles into the vesicle solution, though these can be removed by centrifugation or an extra filtration step. The solid substrate is then incubated with the vesicle solution for at least 20 minutes based on surface plasmon resonance and quartz crystal microbalance studies.⁵⁰ Excess vesicles can be washed away after the incubation. Vesicle fusion usually results in a bilayer with defects or suboptimal surface coverage. However, there are a number of ways to increase the quality of membrane deposited via vesicle fusion technique.³³ Typical preparation methods include incubation with a fresh SUV solution with homogeneous size distribution, coupled with freeze-thaw technique, and then rinsing with solution of a different salt concentration to obtain higher bilayer surface coverage. In particular, the incubation must be performed with a fresh SUV solution because small unilamellar vesicles are unstable and will readily fuse to the clean hydrophilic substrate to make symmetric SLB or to monolayer to create asymmetric SLB.⁵¹⁻⁵² Freeze-thaw cycling will rupture adsorbed vesicles through formation of ice crystals so they can deform and cover the substrate.⁵³ After the incubation, excess and physisorbed vesicles are removed by exchanging the incubation solution with a vesicle-free buffer solution or water. If the rinsing solution has a different salt concentration than the vesicle solution, the concentration gradient creates osmotic

flow which swells or shrinks and ruptures any excess vesicles stuck to the membrane or substrate and thus results in a cleaner supported membrane. This washing step is typically repeated to ensure removal of excess vesicles. After the SLB is deposited on the substrate, thermal cycling/annealing can be done to increase the surface coverage after incubation.⁴⁹

3.2.4. Spreading and Spin Coating Techniques.

Spreading and spin coating are quick and easy techniques for deposition of solid supported lipid membranes. In spin coating, a lipid solution with concentration ranging between 0.25 and 5 mM in a volatile solvent that wets the substrate is deposited on a clean substrate. After spreading, the substrate is rapidly accelerated to a certain rotation speed (e.g. 2000 rpm) to quickly remove the solvent leaving a thin dry lipid film. In the spreading technique, one microliter of lipid solution with a similar concentration range is deposited on a clean substrate and the solvent is allowed to evaporate.⁵⁴ Once a thin, dry lipid layer is formed on top of the solid substrate, the sample can then be partially or fully hydrated to create a stack of lipid membranes. Mennicke and Salditt⁵⁵ described parameters for the spin coating process in detail, such as lipid solution concentration and rotation speed to deposit multiple bilayers (up to 22 layers). Excess floating bilayers can be subsequently removed by a fluid jet to leave a single supported bilayer in the treated region.⁵⁶ The fluid jet is typically water or buffer sprayed onto the substrate from a syringe or MilliQ water dispenser. While this technique can technically be used for solid supported membrane preparation, it is more suited for creating multiple bilayers on a solid substrate. This is due to the numerous defects and low stability of the sample as characterized by various methods such as X-ray reflectivity and electron microscopy.

3.3. Characterization of Solid Supported Bilayers

A solid supported membrane created by any of the methods described above can be characterized by a variety of techniques. Characterization techniques provide information on SLB properties, and the

results from one technique can corroborate data collected by another method. Typically used characterization techniques are described in greater detail below.

3.3.1. Atomic Force Microscopy (AFM).

Atomic force microscopy provides a powerful means to characterize solid supported bilayer systems due to its high-resolution, label-free nature and versatility to work in various environments, including ambient, liquid and culture media.⁶⁻⁷ Local structure and property have been clearly revealed by AFM including topography, domain size, layer thickness, friction, adhesion, and visco-elastic properties.⁸⁻¹¹ The bilayers samples prepared with any deposition technique described previously can be imaged using AFM under one's defined medium. Acquiring AFM images in ambient or nitrogen environment is relatively straightforward. Once the membrane is deposited on a clean surface, the substrate is transferred to a fluid cell specifically designed to hold the substrate under water to retain the native environment of the membrane. The design of the fluid cell is critical for obtaining optimal resolution in the scan. The fluid cell should not hinder the movement range of the cantilever stage and the cell should not couple external vibration to the cantilever. In addition, the cell should also be easy to use and clean.⁵⁷ Depending on the nature of the bilayers, two basic imaging modes have been utilized to characterize the structure and morphology of the bilayers: tapping and contact mode.⁵⁸ Basic rules of thumb for high-resolution AFM imaging of bilayer systems in liquid include: contact mode with soft cantilevers typically yield high-resolution images for gel phases, while tapping mode works better for liquid phase or layers with hydrophilic termini, which tends to adhere to the probes. In contact mode, the tip apex is in firm contact with the surface throughout the scan, while maintaining a set load.⁵⁹ Typically, one could acquire topographic and lateral force images simultaneously. The former reveals the surface contour, while the latter could indicate the functionality, such as hydrophilic versus hydrophobic domains. In tapping mode, the cantilever probe is modulated at resonance frequency of the

cantilever, whose amplitude would decay as the tip approaches the surface. The control electronics maintains the tip-surface separation based on the set damping, e.g. 80% of initial amplitude. Typically, one could acquire topographic and phase images simultaneously. The former reveals the feature heights, while the latter is related to the tip-surface interaction, which in turn depends on the functionality and mechanics of the domain underneath.

For AFM scanning of SLB systems in this work, tapping mode scans were performed with speed of 20 $\mu\text{m/s}$ and tapping amplitude 45 nm at 20% damping. For contact mode, the speed was 20 $\mu\text{m/s}$ and 6.2 nN force. In both cases, the tip used was an AC240 (*Olympus, Japan*) with spring constant of 1.7 N/m.

In addition to imaging, AFM spectroscopy is often used to access the functionality of the features revealed in AFM images. The most known spectroscopy involves the force versus distance measurements, also known as force-deformation profile or curve, from which the adhesive force measured in liquid can be quantified.⁶⁰ With specifically designed modification of the AFM probes, the adhesive force may be correlated to hydrophilicity of the surface feature, DNA hybridization force, specific interactions such as ligand-receptor binding.⁶¹⁻⁶³

Figure 3-2 shows an example of high-resolution topograph acquired using tapping mode. The bilayer consists of an inner monolayer of DPPE, and outer layer of 3:7 1,2-dipalmitoyl-*sn*-glycero-3-phosphoethanolamine (DPPE) – 1,2-dioleoyl-*sn*-glycero-3-phosphocholine (DOPC) lipids. Clearly, phase separation occurs and the morphology is consistent with the known phase separation for DPPE-DOPC bilayers. The DPPE domain in Figure 3-2 appears 1.5 nm taller than the surrounding fluid phase that is made primarily of DOPC.

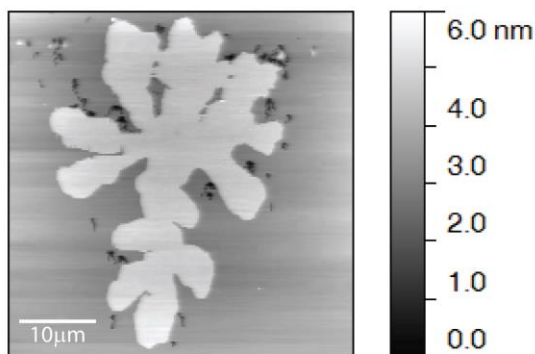


Figure 3-2. 45 μm x 45 μm AFM image of a 3:7 DPPE-DOPC SLB on DPPE covered mica (0001), revealing a gel-phase DPPE domain. The SLB was asymmetric because of the difference between inner DPPE monolayer and outer 3:7 DPPE-DOPC monolayer. Scale bar = 10 μm .

3.4. *Exploration of Ideal SLB Deposition Conditions*

In most cases, a clean, stable, and well-packed membrane is especially desirable for studies involving SLBs. Membrane defects which expose the inner monolayer and holes reaching the underlying substrates are typically present when SLBs are deposited with any commonly used preparation technique. In most cases, these membrane imperfections are nanoscopic and not visible through fluorescence microscopy.⁶⁴⁻⁶⁷ However, such nanoscopic defects and holes can be resolved by high-resolution AFM topography scans and play an important role in altering the molecular structure and behavior of the SLB. Both qualitative and quantitative comparisons of SLBs deposited by various techniques were performed to identify the best procedures and conditions for constructing an ideal system: a stable SLB with minimal defects and holes. Important experimental deposition parameters such as lipid phase state, surface pressure during deposition, packing properties of the inner monolayer leaflet, substrate roughness, and other preparation conditions significantly affect the quality of the resulting SLB. All of these parameters were probed using qualitative observation of the SLB using FM,

quantitative transfer ratio measurements conducted with LB deposition technique, and high-resolution AFM topography to reveal the heterogeneity and coverage.

3.4.1. Quantification of SLB quality by transfer ratio experiments.

An important quantification of the quality of the deposited inner and outer monolayers is a transfer ratio measurement using LB deposition. The transfer ratio is defined as the ratio of area of lipids removed from the air-water interface to the substrate area coated during the deposition. Table 1 summarizes the transfer ratios of various lipid mixtures deposited with LB technique for inner and outer monolayers at 25 °C on different substrates.

3.4.2. Surface chemistry and substrate roughness.

The studied substrates were mica, silicon wafers, and microscope slides (borosilicate glass) to quantify the effect of surface chemistry and substrate roughness on the deposition quality. In general, the transfer of lipid monolayers onto regular coverslip glass resulted in higher transfer ratios than onto mica or silicon wafers. This is likely the result of the significantly larger surface roughness of 8-10 Å root mean square and therefore larger effective surface area vs. silicon wafers (2-3 Å) and mica (0.2 Å). The transfer ratio of pure, fluid and transition phase lipids increased from about 95% surface coverage on mica to ~100% on borosilicate glass. Similar observations were seen for mixed lipid systems containing cholesterol where the transfer ratio increased from less than 90% to about 100%. The only cases where the transfer onto mica was greater were for gel phase DPPE and DPPC. One hypothesis formulated from these observations is that the greater stiffness of gel phase monolayer prevents good conformity and physisorption onto rough glass slides. Conversely, mica's and silicon's ultra-smooth surfaces are especially well suited for transfer of gel phase monolayers. When the monolayer contains cholesterol, or exists at fluid or transition phases, it can conform to roughness of the glass substrate and result in a higher transfer ratio. We also examined the transfer ratio of various lipid mixtures transferred

onto DPPE and DPPC monolayers on both mica and borosilicate glass. However, the inner monolayer always delaminated when it was deposited on borosilicate glass, again reinforcing the need for LS method for the outer leaflet. Thus, outer layer transfer ratios were only done using mica substrates.

3.4.3. *Lipid phase state.*

The phase state of the inner lipid monolayer, which is controlled by the lipid composition and temperature, also greatly affected the transfer ratio of the outer leaflet. The transfer ratio of fluid onto fluid (DTPC on DTPC) and transition onto transition (DMPC on DMPC) were below 80%. However, the transfer of gel onto gel (DPPC on DPPC), gel onto fluid (DPPC on DTPC), and fluid onto gel (DTPC on DPPC) were significantly higher. In addition, gel phase lipids provide a good base for LB deposition of various phase outer monolayers. In some cases, interleaflet lipid coupling enhanced the transfer ratio of the outer layer as can be seen on transfer of DPPC onto DPPC.^{32,37} The coupling condensed the DPPC SLB and resulted in a transfer ratio above 100%. These findings based on transfer ratio experiments about the importance of lipid phase and interleaflet coupling are corroborated using AFM topography scans described in detail in section 4.2.

3.4.4. *Effect of drying the inner monolayer*

Further characterization of outer leaflet deposition was performed on LB deposited DPPE at 45 mN/m with a dipping speed of 1mm/min. We measured transfer ratios of freshly deposited DPPE inner monolayers and monolayers that were dried overnight. If the outer layer deposition was delayed for at least 8 hours after deposition of the inner monolayer, the transfer ratio of outer leaflets were increased for the various types of lipid monolayers. We hypothesize that the drying time between the deposition of the inner and outer monolayer helped to remove trapped moisture on the inner monolayer and trapped between the monolayer and substrate, which would reduce the transfer ratio of the outer monolayer. However, further characterization must be conducted.

Table 3-1. Transfer Ratio Summary of Various Lipid Mixtures deposited with the LB technique.

	Lipid	Deposited on	Phase	Transfer Ratio
Inner Layer	DTPC	Borosilicate Glass	Fluid	102.8 ± 0.7
	DMPC	Borosilicate Glass	Transition (Gel to Fluid)	100.5 ± 0.8
	DPPC	Borosilicate Glass	Gel	89.9 ± 1.0
	DPPE	Borosilicate Glass	Gel	92.0 ± 3.6
	92:8 DPPC-chol.	Borosilicate Glass	Gel	100.1 ± 0.3
	1:1:2 BSM-POPC-chol.	Borosilicate Glass	Liquid Ordered	102.3 ± 3.2
	DTPC	Mica	Fluid	93.4 ± 1.3
	DMPC	Mica	Transition (Gel to Fluid)	95.7 ± 1.1
	DPPC	Mica	Gel	97.2 ± 1.8
	DPPE	Mica	Gel	98.2 ± 1.3
	92:8 DPPC-chol.	Mica	Gel	88.8 ± 3.0
	1:1:2 BSM-POPC-chol.	Mica	Liquid Ordered	80.1 ± 1.8
	DTPC	Silicon Wafers	Fluid	93.7 ± 2.0
	DMPC	Silicon Wafers	Transition (Gel to Fluid)	96.5 ± 0.5
DPPC	Silicon Wafers	Gel	96.2 ± 0.7	
DPPE	Silicon Wafers	Gel	95.9 ± 1.7	
Outer Layer (substrate: mica)	DTPC	DTPC	Fluid	61.7 ± 5.6
	DPPE	DTPC	Gel	96.2 ± 0.4
	DMPC	DMPC	Transition (Gel to Fluid)	75.1 ± 1.8
	DPPC	DPPC	Gel	102.1 ± 0.6
	DTPC	DPPC	Fluid	98.4 ± 0.7
	DTPC	DPPE	Fluid	97.5 ± 1.6
	DMPC	DPPE	Transition (Gel to Fluid)	96.0 ± 1.6
	DPPC	DPPE	Gel	90.5 ± 1.2
	92:8 DPPC-chol.	DPPE	Gel	95.8 ± 0.7
	1:1:1 DPPC-POPC-chol.	DPPE	Liquid Ordered	96.0 ± 1.4
	1:1:2 BSM-POPC-chol.	DPPE	Liquid Ordered	98.6 ± 1.1
	DTPC	Dried DPPE	Fluid	99.0 ± 2.1
	DMPC	Dried DPPE	Transition (Gel to Fluid)	97.3 ± 0.5

DPPC	Dried DPPE	Gel	97.7 ± 2.1
92:8 DPPC-chol.	Dried DPPE	Gel	97.8 ± 0.8
1:1:1 DPPC-POPC-chol.	Dried DPPE	Liquid Ordered	98.3 ± 0.3
1:1:2 BSM-POPC-chol.	Dried DPPE	Liquid Ordered	99.5 ± 1.8

3.4.5. AFM Characterization of Membrane Defects to assess SLB Quality

Another quantification method to assess the quality of the deposited SLB is high-resolution AFM topography scans to quantify nanoscopic membrane defects, which are not resolvable using FM technique. Some of the AFM probed deposition parameters such as lipid phase state, surface roughness, surface chemistry, and interleaflet couplings corroborate the results from transfer ratio measurements and detailed in the following subsections.

3.4.6. Lipid phase state and substrate roughness on the quality of inner monolayer

First, the quality of LB deposited monolayers was determined for various lipids in different phase states at a dipping speed of 1mm/min. These monolayers were scanned using AFM to reveal the presence of holes in the inner monolayer (Figure 3-3). The surface pressure of the LB deposition for each monolayer was chosen where the slope of the isotherm was the steepest for each respective lipid mixture. For monolayers in the gel phase, AFM scans showed that DPPE monolayers had almost no defects across the sample ($\leq 1\%$). The DPPC monolayers also had very few defects, but DPPC monolayers containing 8 mol% cholesterol (at the edge of the gel to liquid ordered phase coexistence region) had a greater number of defects. AFM scans of liquid-ordered 80:20 DPPC-cholesterol showed topographical features with 3-4 Å differences in height, but no defects that spanned across the monolayer. Based on these findings, gel-phase DPPE, DPPC and liquid-order phase 80:20 DPPC-cholesterol would be ideal inner monolayers to construct an SLB. However, exchange between the inner and outer monolayer is likely to occur when the inner monolayer is not in gel phase.⁴⁵ Delamination of the inner monolayer during

deposition of the outer layer can also occur if the physisorption of the inner monolayer is not strong enough. This is the main motivation for choosing LS over LB deposition of outer monolayer leaflets. In the case of mica substrates, the physisorption strength is sufficient to allow LB deposition of both leaflets.

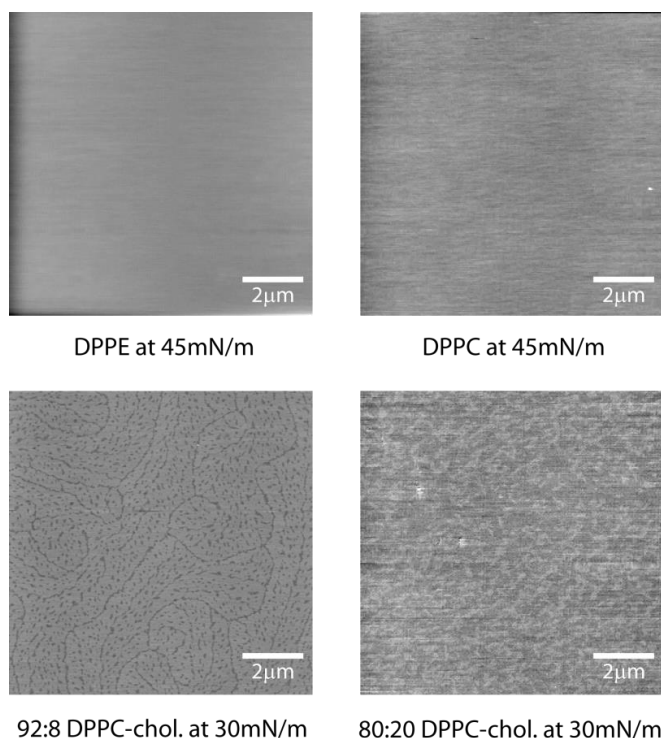


Figure 3-3. Representative 10 μm x10 μm AFM topography scans of various monolayers LB deposited with dipping speed of 1 mm/min on mica. The DPPE and DPPC monolayer were deposited at surface pressure of 45 mN/m and the 92:8 DPPC-chol. and 80:20 DPPC-chol. were deposited at surface pressure of 30 mN/m.

With glass, silica, oxidized silicon wafers, and quartz, the inner leaflet delaminates when attempting to deposit the outer leaflet and LS transfer must be used. In addition, because of mica's low roughness ($\sim 0.2 \text{ \AA}$), SLBs deposited on mica have fewer defects compared to SLBs on silicon wafers or highly polished quartz (Figure 3-4). Quartz and silicon wafers are typically used in ellipsometry and X-ray and neutron reflectivity experiments.

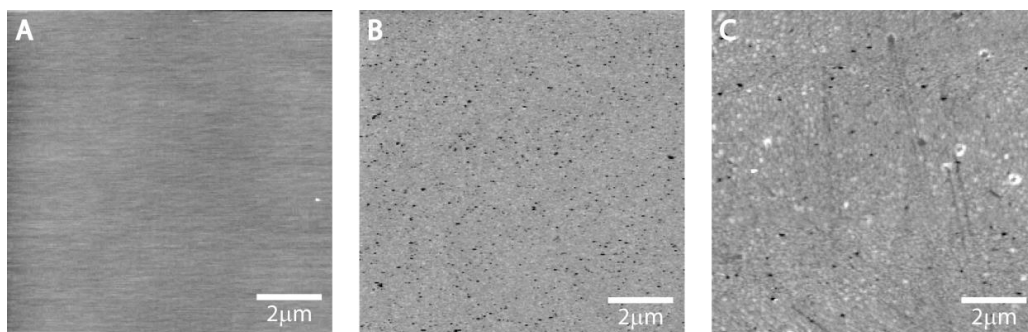


Figure 3-4. Representative 10 μm x10 μm AFM topography scans of DPPC monolayers LB deposited at surface pressure of 45 mN/m on mica (A), silicon wafer (B), and glass slide (C).

3.4.7. Significance of interleaflet coupling and packing of inner monolayer on SLB quality

A previous study by Watkins *et al.*³⁷ used X-ray diffraction to demonstrate the importance of interleaflet coupling between the inner and outer monolayer in the SLB. Thus, the quality of the outer leaflet may, in fact, depend on the completeness of the inner monolayer.⁴⁸ Inter-leaflet coupling and the importance of a well-packed inner leaflet were quantified by characterizing the resulting SLB with a series of symmetric and asymmetric SLB compositions. To minimize the parameter space, two gel phase compositions were studied, DPPC and 92:8 DPPC-cholesterol, which were also scanned as monolayers (Figure 3-3). The symmetric SLBs were prepared using LB-LB deposition at 30mN/m and a dipping speed of 1mm/min for both the inner and outer monolayers. These symmetric SLBs were compared to asymmetric SLBs where the inner monolayer was deposited on a near defect-free DPPE inner monolayer. Figure 3-5 shows the AFM topography scans of the symmetric and asymmetric SLBs. The symmetric SLBs contain more defects than the asymmetric SLBs clearly demonstrating the importance of a strongly physisorbed, defect-free inner leaflet. Because of lower water of hydration, gel phase PE lipids like DPPE are more strongly physisorbed to mica than PC lipids which have about twice the amount of water of hydration per lipid headgroup.³⁰ Consistently, we find DPPC is superior as a base monolayer in “almost” all our studies and yielding a bilayer with fewer topological defects. Moreover,

as demonstrated in numerous measurements of bilayer interactions, the exchange between the inner and outer gel phase leaflet is minimal on mica enabling the interaction of the outer leaflet composition membranes to be precisely determined.^{30, 68-71}

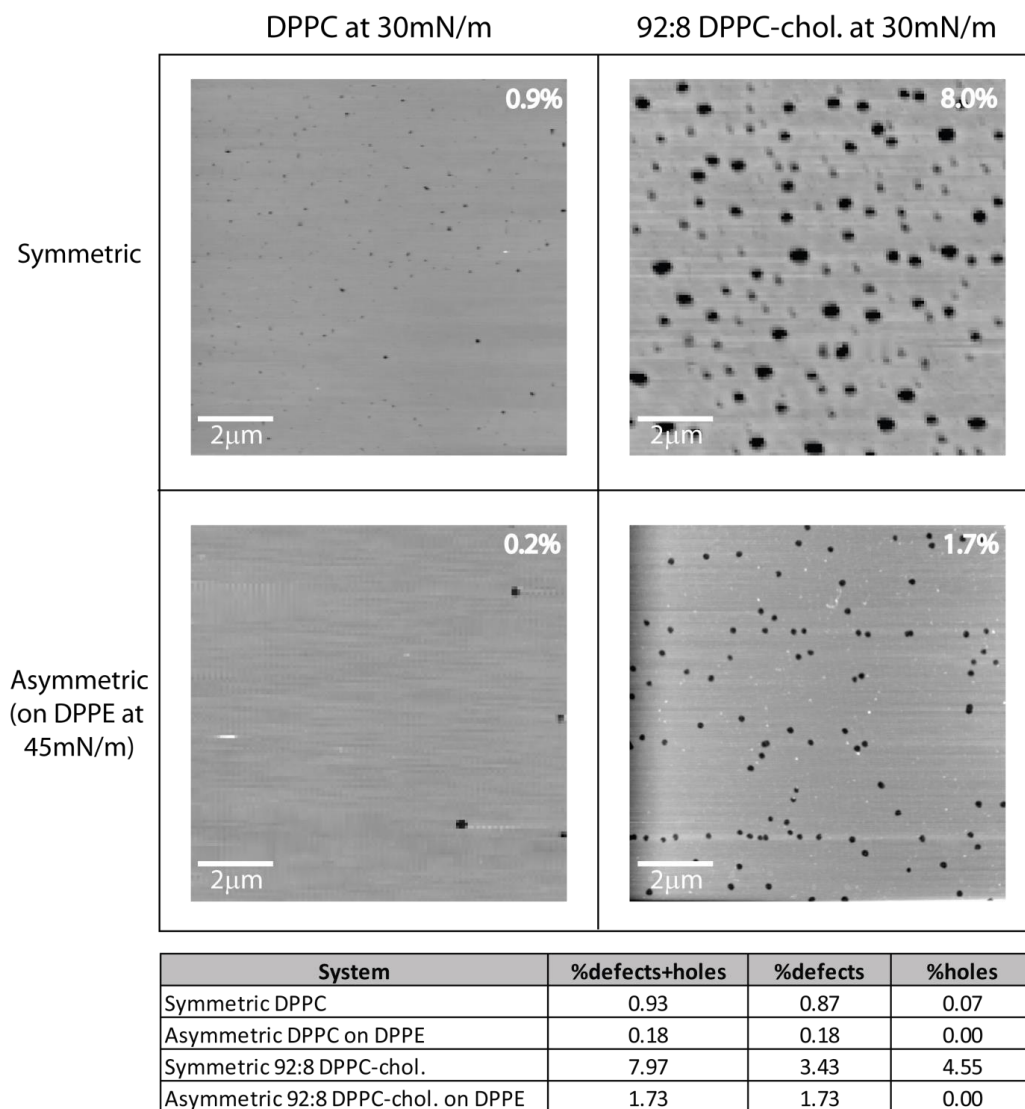


Figure 3-5. Representative 10 μm x10 μm AFM topography scans of DPPC and 92:8 DPPC-chol. deposited as symmetric or asymmetric (on DPPE monolayer) bilayer showing varying amount of membrane imperfections. Defects only span the outer monolayer while holes span the membrane to the underlying support. The number of defects and holes in the table was based on 2-4 samples with at least 5 scans per sample yielding 10-20 analyzed images.

3.4.8. Preparation technique and quality of SLBs

Recent studies of biomimetic “raft” membranes typically involve mixtures of high melting temperature lipids (saturated or sphingomyelin), low melting temperature lipids (unsaturated), and sterols. Depending on the ratio of the components and the temperature, the mixture could exist in gel, liquid order (L_o), liquid disorder (L_d), or multiple phases (i.e. co-existence between L_o/L_d phases) which mimic the liquid-liquid immiscibility region thought to exist in cellular membranes. One frequently studied system is 1:1:1 DOPC-DPPC-cholesterol which makes a uniform fluid phase biomimetic membrane. Using this system, the impact of preparation technique and deposition parameters on the quality of the deposited SLB was investigated. In the first case, we compared hybrid bilayers where the first or inner monolayer was LB deposited near defect-free DPPE (45 mN/m) and the outer monolayer (or leaflet) was deposited by LB, LS, or vesicle fusion. AFM scans of the resulting SLBs clearly demonstrated that LB and LS yield more well-packed, complete membranes (Figure 3-1[E]). The outer layer of fluid phase 1:1:1 DOPC-DPPC-cholesterol was LB deposited at surface pressure of 30 mN/m and dipping speed of 4 mm/min, LS at surface pressure of 30 mN/m, or formed by VF technique 45 minutes incubation using 1 mg/mL SUV solution. In all cases, AFM scans of the resulting SLBs showed nanoscopic monolayer defects down to the inner DPPE monolayer (Figure 3-1[E]). However, the distribution/density and the uniformity of the defects varied depending on the deposition technique. SLBs with an LB-deposited outer layer showed the fewest defects. The quantity of defects increased when LS was used. In LB, the substrate is slowly dipped vertically through the lipid monolayer at air-water interface while maintaining a constant surface pressure. We hypothesize that small lateral defects form either during the deposition process or from a small condensation of the lipids when contacted with the DPPE layer. For the LS technique, the substrate is stamped through the monolayer at the air-water interface. Alignment of the substrate parallel to the monolayer (minimize monolayer film displacement)

is critical to obtain a high-quality transfer. In the case of a VF-deposited outer layer, the quality of the SLB was much worse than an SLB constructed with LB or LS technique. Even though LB and LS showed better quality SLBs, a majority of studies use vesicle fusion as the preparation technique. Qualitative observation with FM revealed that the VF deposited membranes contained microscopic defects ($>1 \mu\text{m}$) and generally were less homogeneous, particularly in preparing asymmetric SLBs (Figure 3-1). Moreover, the quality of the hybrid SLB form when vesicles fused to an LB deposited monolayer had significantly less uniformity than when vesicles were fused to a bare substrate. In addition, nanoscopic membrane defects also exist. Finally, excess vesicles are hard to completely remove from the system, and the lack of control over the deposited membrane's surface pressure makes VF inferior to the LB and LS techniques. Still, VF is the most straightforward method to make SLBs and the only method that can be used to perform backfilling for membrane lithography (filling up defects or areas with no bilayer or only a monolayer on the surface).⁷²

3.4.9. Cholesterol in altering the phase state and SLB quality

Cholesterol, a specific type of sterol, is known to alter the packing or phase of 1,2-dipalmitoyl-sn-glycero-3-phosphocholine (DPPC) monolayers. The transition between the gel and liquid order phase occurs at ~ 15 mole% cholesterol. In order to study the effect of cholesterol and phase state on the quality of LB deposited SLBs, binary mixtures composed of DPPC with various cholesterol concentrations were deposited on a robust, near defect-free DPPE inner monolayer (Figure 3-6). As the amount of cholesterol increased from 0-20 mole%, the mixed monolayer gradually transitions from a pure gel phase to a binary coexisting phase of gel and L_o . AFM scans showed that as the gel phase monolayer became more fluid, more defects were observed. Similar effects of increasing defect density with higher fluidity can be observed for any mixture of lipids, and thus LB and LS deposition are typically performed with the lipid

mixture in the gel or solid phase state. Another advantage of deposition with gel phase systems is a lower flip-flop rate between the inner and outer leaflet, and a slower equilibration process (lipid dissolution into the subphase). Presaturating the working solution with lipids in the outer leaflets minimizes desorption for longer time experiments.

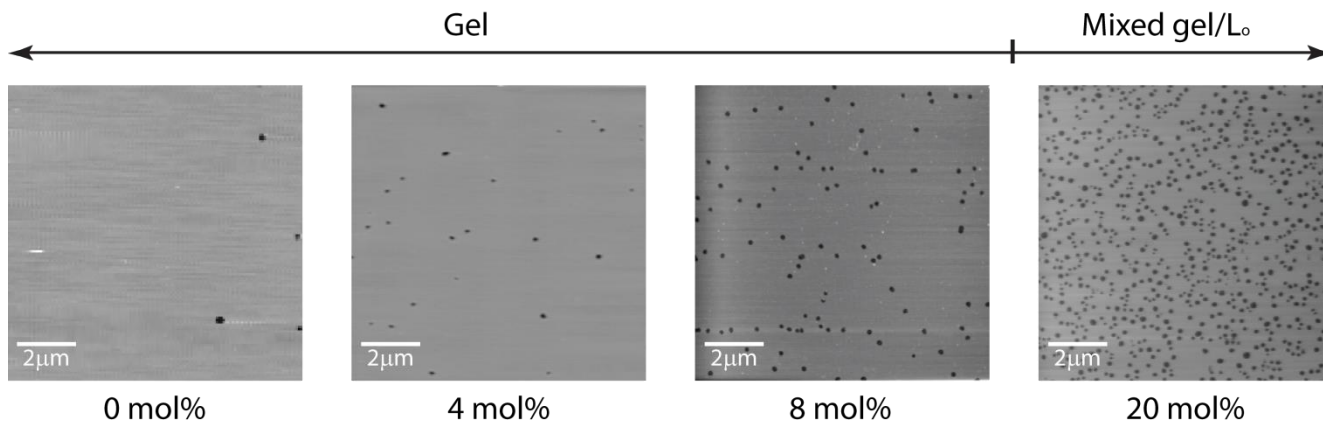


Figure 3-6. 10 μm x 10 μm AFM topography images showing defect density as function of cholesterol concentration in a DPPC outer leaflet at 25 °C. The outer monolayers were deposited on a near defect-free DPPE inner monolayer on mica.

3.4.10. Surface pressure/area per molecule.

Another important deposition parameter that dictates the quality of the resulting SLB is the surface pressure during deposition. The surface pressure-area (Π -A) isotherm depends on the lipid mixture and temperature, and can be used to select the desired lipid packing (area per molecule) of the deposited monolayer. Typically, deposition using LB or LS technique is conducted with a surface pressure where the slope of the Π -A isotherm curve is at its steepest (largest change in the surface pressure with small shift in area per molecule). The surface pressure is held constant during the deposition by decreasing the area of the monolayer film as material is transferred from the air-water interface to the substrate. Better uniformity and transfer occurs when the change in pressure is large for a small change in area. For this reason, layers cannot be transferred well in the coexisting regions and

better transfers are typically obtained in the solid or gel phase state. The relationship between the surface pressure (or area per molecule) and amount of membrane defects/holes in the deposited monolayer can be observed experimentally by AFM topography scans of LB-deposited 92:8 DPPC-cholesterol mixtures at various surface pressures. Figure 3-7 shows the pressure-area isotherm of 92:8 DPPC-cholesterol at 25 °C and AFM scans of the hybrid SLB composed of 92:8 DPPC-cholesterol deposited on DPPE at various surface pressures. In all cases, the dipping speed was 1mm/min and the DPPE inner leaflet was deposited at 45 mN/m on mica. The SLB deposited at 30 mN/m shows the smallest defect size and lowest defect density. The higher total defect density and larger defect size at 40mN/m is attributed to the lower stability of the monolayer at this surface pressure where the slope of the Π -A curve is beginning to decrease. At the lower surface pressure of 20 mN/m, again a larger defect size and density occurs. One might hypothesize that the greater defect density at 20 mN/m compared to 30 mN/m is due to condensation of the deposited film and potentially driving to a more equilibrated state. However, a careful GIXD of pure DPPC membranes LB/LS deposited as a function of surface pressure on quartz demonstrated that these gel phases SLBs for the most part tracked and maintained the conditions under which they were deposited.^{32,37} Subtle changes were observed between monolayers and bilayers because of coupling between the leaflets, but to first order the packing and structure of the SLB followed the deposition pressure consistently.

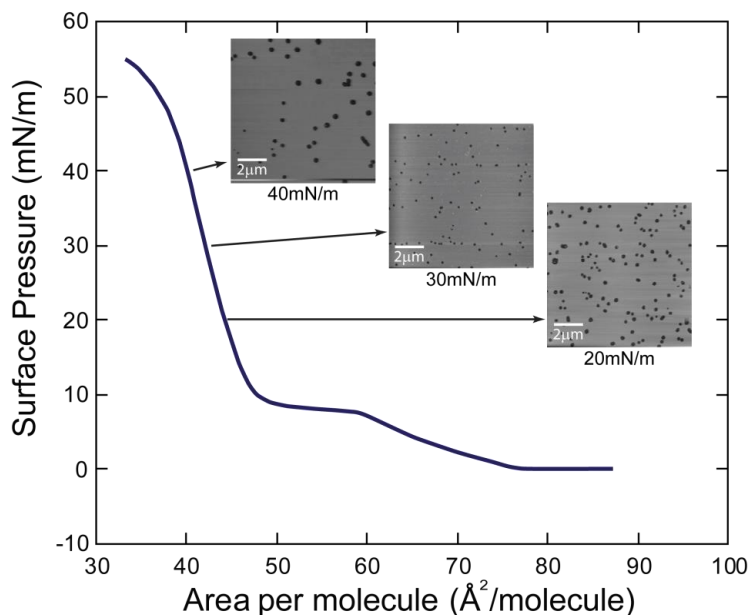


Figure 3-7. Effect of surface pressure on defects in LB deposited 92:8 DPPC-cholesterol on DPPE. Insets are 10 μm x 10 μm AFM topograph at surface pressure of 20, 30, and 40 mN/m, respectively. The outer leaflet was deposited at dipping speed of 1 mm/min and 25 $^{\circ}\text{C}$.

3.5. Conclusion

The solid supported bilayer is a simple and robust platform which is extensively used to obtain biomimetic lipid membrane properties such as lateral topography, lipid mixing and phase state, dynamics/diffusion, as well as a base system for studies with proteins and other molecules of interest using various complementary characterization techniques. This instructional review discussed different preparation techniques to create SLBs with an emphasis on parameters and conditions that yield the highest quality bilayer. Membrane imperfections, such as holes that reach down to the substrates or defects which extend down to the inner SLB leaflet were characterized. Some experiments using the SLB platform require a specific type of lipid mixture. Optimal deposition parameters such as lipid phase, surface pressure, inner leaflet packing, and substrate roughness were described in detail to aid in creating the best quality SLB for the desired studies. Comparisons of SLBs prepared with different methods were performed qualitatively by fluorescence microscopy, and quantitatively by transfer ratio measurements

and high-resolution AFM topography scans. In general, SLBs prepared by LB-LB and LB-LS techniques are superior compared to vesicle fusion because of the lower defect density and absence of residual vesicles, which are undesirable for some characterization or subsequent measurement techniques. In addition, LB and LS deposition are further preferred as the surface pressure and packing area can be controlled. The SLB can also be modified by incorporating various molecules such as membrane proteins, and used to probe the inserted molecules. However, the study of membrane proteins on SLBs is limited to peripheral membrane proteins or integral membrane proteins that do not protrude out from membrane. The absence of a water cushion between the SLB and substrate frequently denatures transmembrane proteins resulting in their loss of function. The optimal deposition parameters for SLB are also relevant for polymer-cushioned SLBs, which are an extension of the SLB platform used for transmembrane protein study.

3.6. Acknowledgements

Most of the work described in this chapter was submitted to Langmuir, and is currently under review. If accepted, the text and figures can be used with permission from ACS (see url: <http://pubs.acs.org/pb-assets/acspubs/Migrated/dissertation.pdf> for copyright policy). The results reported in this chapter was a collaborative work with James Kurniawan, coordinated the films preparation, isotherm acquisition, fluorescence imaging, and transfer ratio determination. This work was primarily supported by the NSF chemistry division through grant CHE-1413745 and CHE-1413708, and Betty and Gordon Moore Foundation. Special thanks to thank Alan Hicklin and Keck Spectral Imaging Facility for AFM usage; Yeeun Kim for the assistance with AFM sample preparations; Amanda Dang, Hilary Chan, Gregory Kittleson, and Shawn Mattathil for assistance with transfer ratio and fluorescence microscopy experiments.

CHAPTER 4

DEVELOPMENT OF A NEW METHODOLOGY FOR BUILDING THREE-DIMENSIONAL NANOSTRUCUTRES

4.1. Introduction

Three-dimensional (3D) printing is among the most active areas of research and development (R&D) in current industry⁷³⁻⁷⁴. While commercial 3D printers enable production of materials by designed geometry, none is able to produce nanostructures, which requires ultra-high spatial precision. The lack of spatial precision is due to the intrinsic limitations of current 3D printing: lack of precision in movement and difficulties in delivery of ultrasmall amounts of materials. Thus, they are unable to reach nanometer accuracy. In principle, 3D nanoprinting should fulfill the following technical requirements: (a) nanometer precision in both positioning and material delivery; (b) 3D custom-design support; and (c) ease of use with practical throughput. Scanning probe microscopy (SPM) based lithography is known for its nanometer accuracy in imaging and 2D lithography^{2, 75-77} due to the precision positioning by piezo mechanics and nanometer sharp probes. Prior studies on the development of 3D nanoprinting via SPM include dip-pen nanolithography in association with Langmuir Blodgett (LB) film deposition. By contact between the AFM tip and substrate, a 3-layered structure was produced with an overall height of 6 nm, and a single layer diameter as small as 250 nm.⁷⁸ AFM-based sculpting via thermal decomposition has been reported with a lateral resolution of 15 nm and an overall height of 20 nm.⁷⁹ Mechanical shearing has also been performed to create nanoscale features. For example, shaving away layers of thiols was used to create a square-shaped negative feature with a maximum depth of 8 nm.⁸⁰ 2D nanolithography in conjunction with pattern transfer has also been performed to build 3D nanostructures.^{1, 3, 81-83} To truly achieve layer-by-layer deposition, improvements in spatial movement and material delivery are necessary. Our recent efforts demonstrated that true 3D printing could be achieved using AFM based

technology and polyelectrolyte materials.⁴ This paper reports a similar approach but with a different material, photocurable, polymers, which is significant since it demonstrates the versatility of our methodology with materials that can be cured to yield a wider range of material properties.

4.2. Materials and Methods

4.2.1. Materials

The material chosen for this work was a UV curable polymer, Loctite®349™ (Henkel, Germany). This material is composed of methacrylate esters and polymerizes at a wavelength of 365 nm. The curing of the polymer was conducted in real time using UV light as the polymer was delivered to the substrate.

4.2.2. Preparation of substrate

Silicon wafers were prepared with a cleaning process of immersion in *Piranha* solution for 1 hour and rinsing with copious amounts of water. The wafer was then dried with a stream of nitrogen. Substrates were prepared and used the same day to guarantee a clean surface at the nanoscale.

4.2.3. AFM

A MFP-3D-Bio AFM (Oxford Instruments, Santa Barbara, CA, USA) was used to perform the delivery of the polymer to the substrates. An AC240 (Olympus America, Central Valley, PA, USA) cantilever with a 2 N/m spring constant was chosen to carrying the polymer and image the resulting produced features. The delivery step was conducted using a force of 2.4 μN while the imaging was performed with a force of 2.3 nN using the same tip. The only factor that differed in the delivering and imaging was the force applied to the cantilever. For both processes, the speed was 6.4 $\mu\text{m/s}$.

4.3. Results

4.3.1. 3D printing of line arrays

An essential feature of a 3D printer is the ability to deliver multiple layers of material, resulting in a stable structure with 3D aspect. In order to show this capability, various lines with different numbers of passes of the AFM tip were printed on the surface of silicon. Figure 4-1 shows the resulting lines composed of 40, 30, 20, 10, 4 and 2 passes and the corresponding heights of 4.1, 2.7, 1.9, 1.7, 1.1 and 0.5 nanometers, respectively. The widths of the lines were 160, 140, 120, 130, 120 and 100 nanometers, respectively.

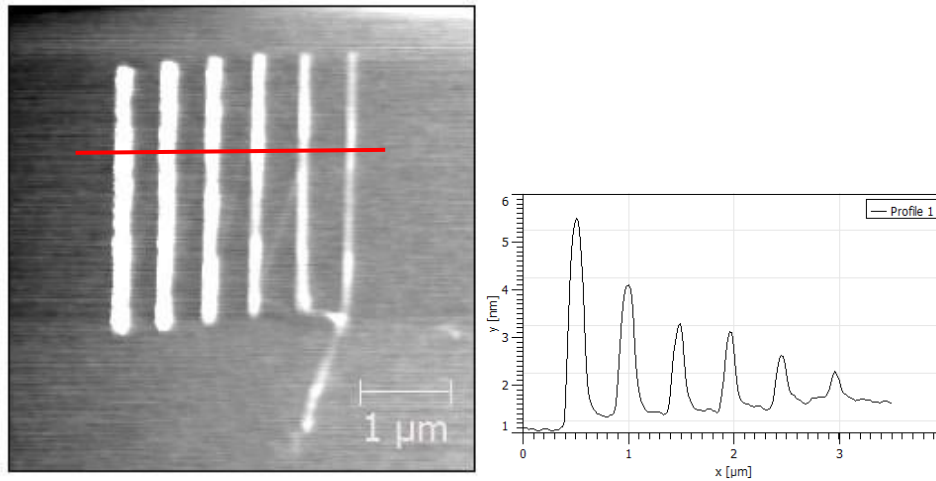


Figure 4-1. A 5x5 μm AFM topographic image revealing 6 lines printed on a Si(111) wafer surface. The lines were composed of different numbers of passes of the AFM tip. From the left to the right: 40, 30, 20, 10, 4 and 2 passes. The height of those lines varied in accordance with the number of passes. From the left to the right the heights were: 4.1, 2.7, 1.9, 1.7, 1.1 and 0.5 nanometers.

These results showed the ability of this method to deliver the polymer and cure on the surface. This process enables the stacking of multiple layers of polymer, resulting in multilayered (3D) structures.

4.3.2. 3D nanoprinting retains the fidelity of the design

Another important feature of a 3D printing method is the ability to produce custom design features. In Figure 4-2, two parallel lines were printed with a 500 nm gap between them. A crossing line at 45° was then printed on top of the parallel ones. All the lines were printed with 20 passes of the AFM tip. Cursor 1, crossing the two parallel lines, showed a height of 0.9 nm and a width of 160 nm, respectively. Cursor 2, crossing the intersection of the lines, shows the stacking of the lines, i.e. a height of 2.0 nm. It is clear that the protocols used here enable the printing and curing in time to support the design of stacked line features.

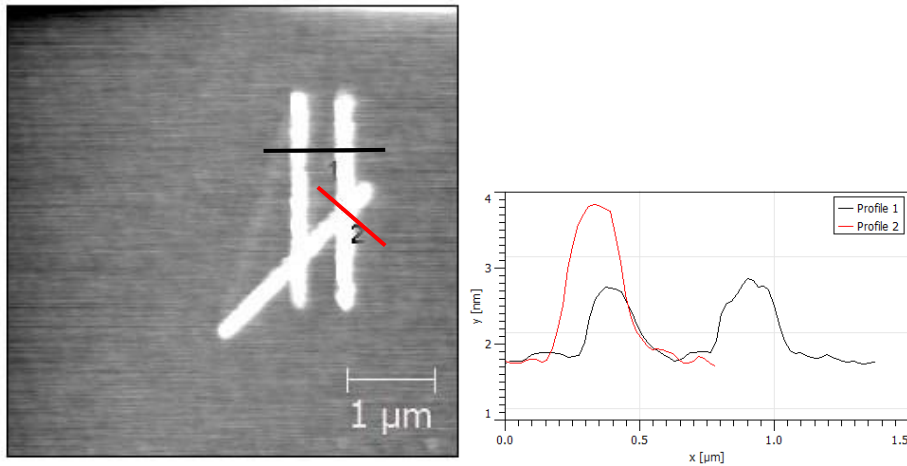


Figure 4-2. A 5x5 μm AFM topographic image revealing 6 lines printed on a Si(111) wafer surface. The lines were each produced by 20 passes. Cursor profiles allow measurements of line height and width at the defined locations.

4.3.3. 3D printing of stacked grids

A more complex design was produced by printing 10 lines 500 nm apart from each other, then another 10 lines, (also with 500 nm spacing between each other) perpendicular to the previous printed ones, and a third set of 10 lines printed on top of the first set of lines. All the lines were printed with 2 passes of the AFM tip. The resulting structure, shown in

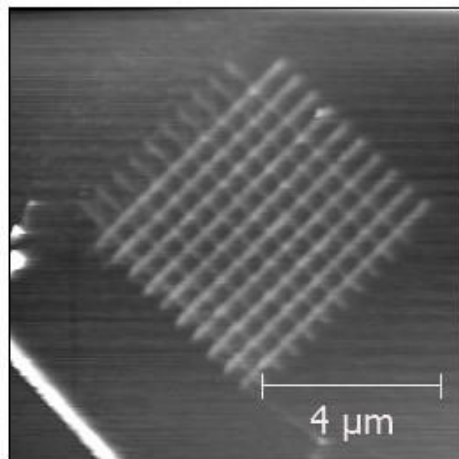


Figure 4-3. A 10x10 μm AFM topographic image revealing 6 lines printed on a Si(111) wafer surface.

Figure 4-3, is a grid of lines composed of a set of single layer lines with a height of 0.4 ± 0.1 nm; a set of lines of 2 stacked layers with a height of 0.9 ± 0.1 nm; and the crossing points of the two sets of lines, composed of three layers of the polymer with a height of 1.2 ± 0.1 nm. The production of this grid showed the ability to fabricate custom structures with complex designs, composed of multiple layers with nanometer precision. The crossing lines do not span or form a bridge between the parallel lines, but were delivered on the bottom lines and in between the gaps on the bottom, or in the valleys, between the existing lines.

4.4. Conclusion

Using a photopolymer and AFM-based delivery methodology, we have demonstrated that photocurable polymer materials may be printed layer-by-layer. By controlling the number of passes, we could control the height of features with nanometer precision. The fidelity was high and enabled specific designs to be followed with excellent homogeneity within the lines printed. Work is in progress to further improve spatial precision and to produce more complex designs.

4.5. Acknowledgements

Most of the work described in this chapter was presented in **2016 IEEE 16th International Conference on Nanotechnology**, and published on IEEE-Nano. The text and figures are used with permission from IEEE (see url: https://www.ieee.org/publications_standards/publications/rights/rightslink_usetypes.html for copyright policy). This project was funded by National Science Foundation (NSF), Conselho Nacional de Desenvolvimento Científico e Tecnológico (Brazilian National Council for Scientific and Technological Development), and Gordon and Betty Moore Foundation.

CHAPTER 5

THREE-DIMENSIONAL NANOPRINTING USING DIRECT DELIVERY

5.1. Introduction

In the fields of 3D writing and additive manufacturing, the direct delivery method produces 3D structures with feature sizes down to the micrometer scale.⁸⁴⁻⁹⁷ Direct writing methods produce structures by the extrusion of ink in the fluid state through a nozzle, followed by curing to retain shape. The inks suitable for this method are typically composed of particulate and polymeric materials that are suspended or dissolved in a liquid solvent. Alternatively, a solid ink is heated to the fluid state to be extruded and molded. The advantages of direct delivery include applicability to a wide range of materials, simplicity, and low costs as additional stimulation (photo, electric or thermal) is not necessarily required.⁹⁸⁻¹⁰² While 3D nanoprinting via direct delivery is becoming routine with millimeter precision, further miniaturization is challenging as modern applications require small feature size, sub-micrometer to a few nanometers.¹⁰³ Examples of applications addressed with 3D printing include nanophotonics,¹⁰⁴⁻¹⁰⁷ nanoelectronics,¹⁰⁸⁻¹⁰⁹ micro- and nano-fluidic devices,¹¹⁰⁻¹¹¹ catalyst supports,¹¹²⁻¹¹⁴ filtration media,^{103, 115} semiconductors,⁸⁷ and tissue engineering scaffolds.^{28,29} Current technology effort has pushed the feature size to 1 μm using small injection systems and advanced polyelectrolyte chemistry.⁴ Further miniaturization is increasingly difficult because of the spatial accuracy required for both reproducible positioning and material delivery.

We report our direct delivery system for miniaturizing 3D printing using a high precision positioning system coupled to atomic force microscopy probe-based nanofluidic delivery. Layer-by-layer deposition to produce distinct geometries is achieved with 4.8 nm precision over 1 mm overall object size.

5.2. *Experimental*

5.2.1. *Materials*

Reagents were used without further purification unless described specifically. Sulfuric acid (95.0%), hydrogen peroxide (30% aqueous solution) were purchased from EMD Chemicals (Gibbstown, NJ, USA). Gold slugs (99.999%) were purchased from Alfa Aesar (Ward Hill, MA, USA). Deionized and ultrapure water was attained from a Milli-Q water system (EMD Millipore, Billerica, MA, USA). The photopolymerizable material used was Loctite® AA 349™ (Henkel, Germany). This commercially available adhesive is composed of a mixture of methacrylate esters that polymerizes when exposed to UV radiation of 365 nm. It has a transparent appearance and a viscosity in the range of 6,000 to 13,500 mPa.s (cP) at 25°C. The 1" x 3" glass slides (Fisherfinest Premium, Fisher Scientific, Pittsburgh, PA, USA) were immersed in Piranha solution, which consists of 3 parts of sulfuric acid to 1 part of hydrogen peroxide 30%, for 2 hours. The clean glass slides were rinsed with MilliQ water and dried under a constant flow of nitrogen for 5 minutes.

5.2.2. *Scanning electron microscopy Imaging.*

The hierarchical 3D structures produced are characterized using scanning electron microscopy (SEM). To avoid charging, a thin layer (4 nm) of gold was deposited onto the glass slide, coating the printed structures, using a high-vacuum evaporator (DV502-A, Denton Vacuum, Moorestown, NJ, USA), at a base pressure below 2×10^{-6} Torr and evaporation rate of 1.5 Å/s. SEM images were acquired on a Hitachi S-4100T FE-SEM (Hitachi High Technologies America, Inc., Pleasanton, CA, USA), using an accelerating voltage of 2 kV at 10 μA.

5.2.3. Atomic force microscopy imaging

AFM images were acquired with a MFP-3D atomic force microscope (Asylum Research, USA). Probes (AC240, Olympus, Japan) of 1.7 N/m spring constant and 57 kHz resonant frequency were used in contact mode to check the integrity of the printed structures with a force of 55 nN. Tapping mode was used at 80% damping of a 1 nm free amplitude oscillation for all the other scans, in order to minimize disturbance to the fabricated features. Images were processed using Gwyddion open source software, which is freely available on the Internet and supported by the Czech Metrology Institute.

5.3. Results and Discussion

5.3.1. AFM-based nanofluidic device for delivery.

The printing process was carried out combining an AFM and microfluidic platform (FluidFM BOT, Cytosurge, Glattbrugg, Switzerland) as illustrated in Figure 5-1[A]. The precision movement stage is mounted onto an inverted optical microscope (IX-73, Olympus America, Center Valley, PA) to monitor the position and delivery. The XY-movement ranges 240 mm x 74 mm, with a precision of nanometers; and the Z-movement is independent from lateral movement with nanometer precision over 50 mm. The support for 3D nanostructure is placed on the XY stage, while the probe is mounted to vertical assembly controlling z-movement. The AFM probes used in this work differ from conventional microfabricated AFM probes because they also serve as microfluidic delivery. A typical probe is shown in Figure 5-1[B] (FluidFM Nanopipette, CYPR/001511, Cytosurge, Glattbrugg, Switzerland), where the cantilever is similar to typical AFM probes made of Si, 200 μm long, 36 μm wide, and 1.5 μm thick. The spring constant is 2 N/m. The pyramidal tip has a square base with side length of 10 μm , and 7 μm in height. Important to material delivery, the pore, 300 nm diameter, represents the end of a microchannel within, and is located at the center of apex. The microchannel is connected to a small

reservoir where the printing materials reside, and a mechanical pump and control system enable pressure application -800 to 1000 mbar with 1 mbar precision.

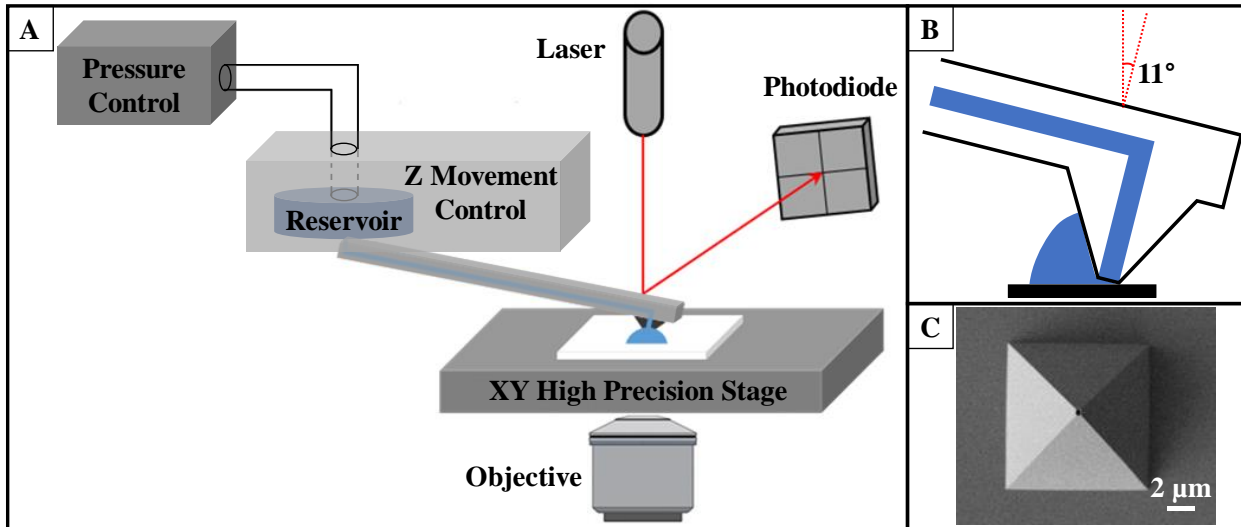


Figure 5.1. [A] Schematic diagram of the key parts of the combined AFM and microfluidics for 3D nanoprinting. [B] SEM image of the microfluidic AFM cantilever used in this work. [C] A zoom-in view of the tip apex showing the size of the opening atop.

5.3.2. 3D nanoprinting of stacked grids

The design of the 3-layer stacked grids is shown in Figure 5-2. A grid of overall dimension 1mm x 1 mm was constructed from a pattern of 51 lines at a period of 20 μm . Three superimposed layers were constructed in this manner, each layer composed of a single pass of the probe. The first and third layers of lines had the same orientation so the lines were superposed on each other; the 51-line pattern of the second (middle) layer was written perpendicular to the other two layers.

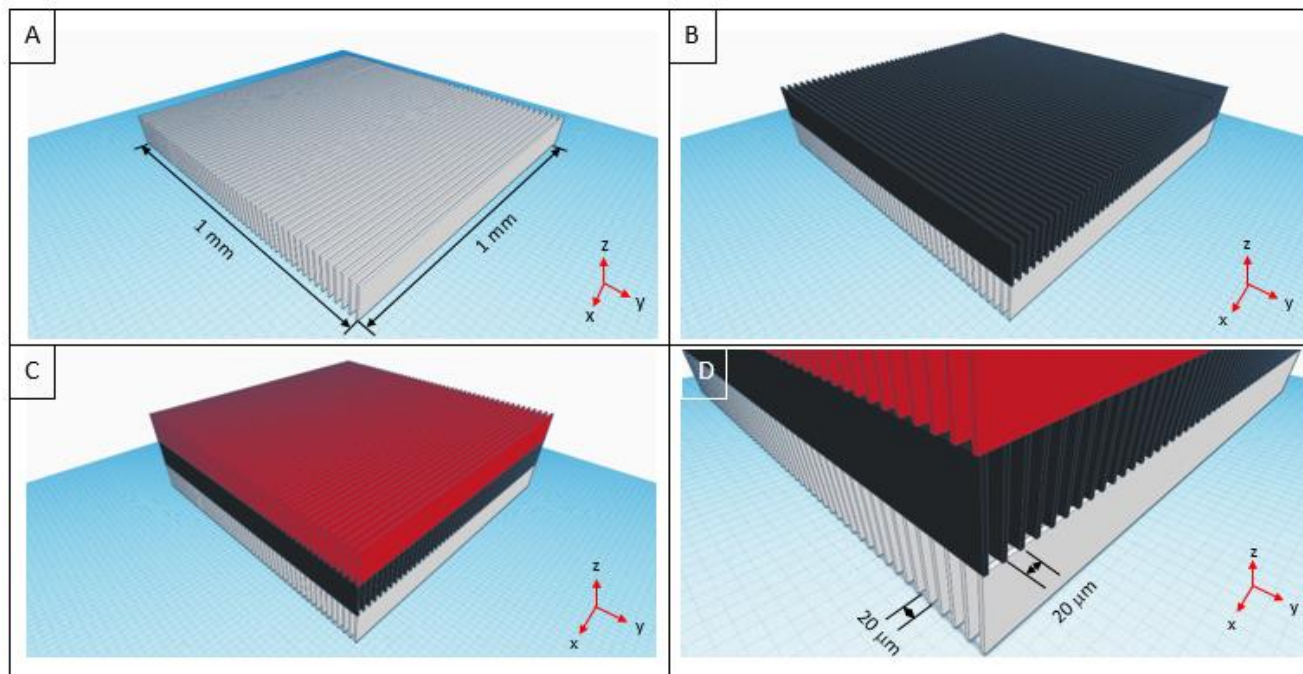


Figure 5-2. Schematic diagram of the printed grids. [A] The first layer (grey) is the base of the stack with overall dimensions of 1mm x 1mm. [B] The second layer (black) lies on top of the first layer and is oriented perpendicular to the first set of lines. [C] The third layer (red) lies on top of the second layer and is perpendicularly oriented with respect to the second layer; hence, it has the same orientation as the first layer. [D] Zoom-in of the grid showing the 20 μm periodicity of the lines

In the printing process is to load the ink into the probe reservoir with a 1 μL syringe (Hamilton, Reno, NV, USA). Optimal conditions were determined by controlled systematic trials in which pressure, speed and set point were varied to find the most reliable conditions to deliver the minimum amount of ink. Extrusion pressure was kept constant at 200 mbar throughout the printing process. The speed of printing while the probe was in contact with the surface was 50 $\mu\text{m}/\text{s}$, and the force set point was 20 nN. After the printing step, the glass substrate containing the printed 3D structures was exposed to 365 nm at 40 mW/cm^2 radiation for 15 minutes to assure complete curing.

The final structures were characterized with SEM to visualize the overall structure within one image frame. Prior to SEM imaging, the samples were coated with a 4 nm layer of gold following the procedure stated in the experimental. The glass slide was then cut into a 1 cm x 1 cm square, mounted to the SEM sample holder and transported into the vacuum chamber. The images were acquired using an accelerating voltage of 2 kV at 10 μ A.

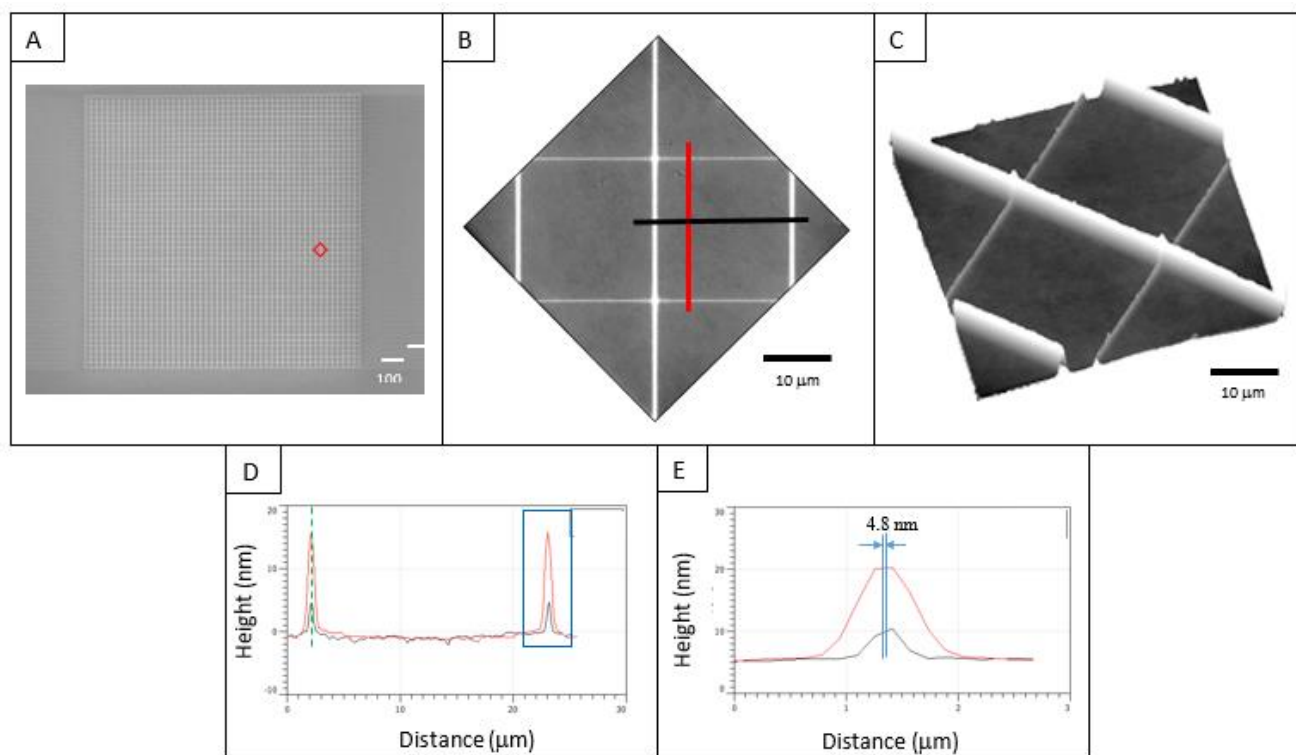


Figure 5-3. [A] A 1.1 mm x 1.4 mm SEM image showing the 3-layered printed grid. [B] a 40 μ m x 40 μ m AFM topographic image to reveal the detail of the grid region of the red box of (A). [C] 3D rendition of the AFM topography image of (B). [D] 2 cursor profiles as indicated in (B): the red cursor crosses the superimposed 1st and 3rd layer of the grids, and the black cursor crosses 2 lines in the 2nd layer of grids. The left peaks are superposed ($\Delta x = 0$), so the precision in the superposition

of the peaks in the right can be determined. [E] A zoom-in view of the right peak in (D). The center of the grids is aligned with 4.8 nm precision.

A SEM image of the grid (Figure 5-3[A]) displays the overall pattern with lateral dimensions of 1 mm x 1 mm. The stacked grids appear uniform over the entire region with little distortion or misposition. More detailed structural information was provided by AFM in Figures 5-3[B-E]. Using contact mode at a load of 55 nN, and scanning speed of 5 $\mu\text{m/s}$, the AFM topography shown in Figure 5-3[B] clearly reveals the dimensions of the individual grid features. Figures 5-3[B] and 5-3[C] are AFM topographic images of a 40 μm x 40 μm area rendered in two- and three-dimensional views, respectively, illustrating the difference in height between the grids with 1 and 2 passes. Figure 5-3[D] aligns two cross-sectional lines with each other to demonstrate the precision of interline spacing. The cursor profiles shown as black and red lines in Figure 5-3[B] are displayed in Figure 5-3[D]: the black cursor crossing two grid lines made by a single pass shows heights of 5 and 6 nm and full width at half maximum (FWHM) of 310 and 330 nm, respectively. The red cursor crossing the two grid lines composed of two passes shows a height of 16 nm for both lines and FWHM 680 and 740 nm, respectively. The non-additive characteristic of the heights of these lines is due to the difference in the interactions between substrate/ink (first pass) and ink/ink (second pass). In all cases, the second pass is observed to promote the delivery of a higher layer and that is credited to the greater interaction between the first deposited layer of ink when compared with the bare substrate. There is no observed offset between the 1st layer and 3rd layer grids, as shown in the red cursor, indicating the accurate alignment of our system. Figure 5-3(E) magnifies the cross-section of two superimposed lines (layer 1 and layer 3) to demonstrate the precision of 4.8 nm in repeatably returning to the same feature to deposit subsequent layers. This precision remains true for all the grids produced in Figure 5-3, which demonstrated little distortion along both directions. This 4.8 nm spatial accuracy along 1 mm dimension is among the highest precision

reported. The experiments shown in Figure 5-3 were reproduced 4 times, and the FWHM attained in the first layer of grids ranged from 310 to 370 nm. The height ranged from 4.8 to 6.0 nm. The FWHM of grids made of 2 passes measured 490 to 740 nm with a height of 14.0 to 17 nm.

The effect of printing speed was measured over 4 lines printed at 50 $\mu\text{m/s}$ and 4 lines printed at 200 $\mu\text{m/s}$. The lines produced at the faster speed had FWHM that ranged from 500 nm to 600 nm for a single layer lines and 600 nm to 800 nm for 2 layer lines. The heights of those lines ranged from 3.3 nm to 4.0 nm for single layer lines and 7.5 nm to 11.3 nm for 2 layer lines. The decrease in height is attributed to a shorter dwell time for the fabrication of each line. Less material is delivered and consequently the lower height is observed. The precision in the superpositioning of lines was 5.2 nm in this case.

5.3.3. 3D nanoprinting of complex structures by design.

The ability to produce 3D structures by custom design is illustrated in the printing of a four-leaf clover at various sizes in a layer-by-layer process illustrated in Figure 5-4. The outline of the leaf is made of 3 rounds of delivery of the ink from the microfluidic AFM probes. The overall size is indicated by dimensions marked as a and b.

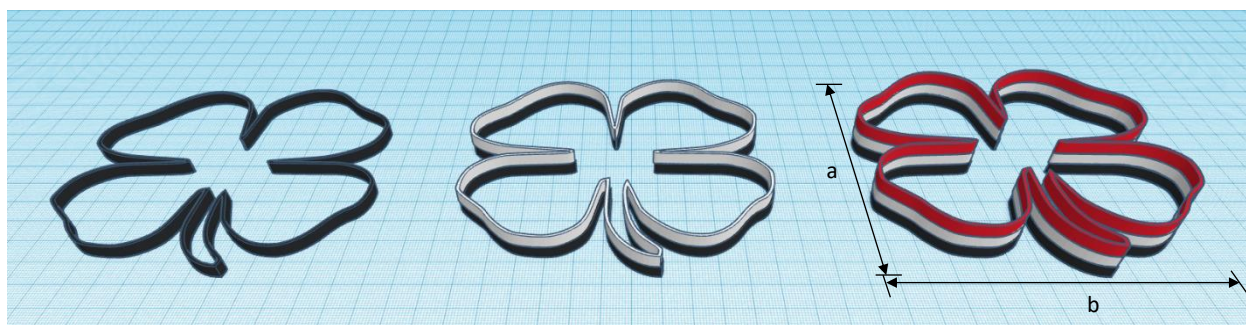


Figure 5-4. Schematic diagram of the process of printing a 3-layer four-leaf clover: layer one shown in black, layer two in gray, and layer three in red.

Seven clovers were printed with seven sets of a and b values, all at the same aspect ratio of a:b = 1.15, summarized in Table 5-1.

Table 5-1. Lateral dimensions of seven clovers printed in the scheme of Figure 5-4. For all clovers, the ratio of dimensions is constant, a/b = 1.15.

<i>Clover #</i>	<i>a (μm)</i>	<i>b (μm)</i>
1	1500	1300
2	750	650
3	375	325
4	190	165
5	95.0	82.0
6	50.0	43.0
7	5.00	4.30

The ink was loaded into the probe reservoir and the extrusion pressure was kept constant at 200 mbar throughout the printing process as described above for constructing the stacked grids. The speed of printing while the probe was in contact with the surface was 50 μm/s, and the force set point was 20 nN. Similarly to the grid structures, the glass substrate containing the printed 3D structures was exposed to 365 nm at 40 mW/cm² radiation for 15 minutes to assure complete curing. Figure 5-5[A] shows an SEM image of clovers 1-6, where the design is clearly followed qualitatively and quantitatively. There is little distortion or fuzziness of the lines. In the largest leaf, a = 1.500 mm and b = 1.300 mm, in accordance with the design. The line width for this structure is 450 nm, indicating clear overlap for all three layers. Clover #6 is not clearly resolved in this SEM image, and we show its AFM topograph in Figure 5-5[B], where the 3D structure is clearly visualized, a = 50 μm, b = 43 μm. The FWHM ranged

from 410 to 470 nm. The heights ranged from 9 to 11 nm, where left edges are systematically taller than the right. This observation is explained by the non-symmetric contact of the probe apex with the surface. The 11° default angle with which the probe is positioned onto the surface causes the extrusion of material to vary depending on the printing direction. The smallest feature, clover #7 is shown in figure 5-5[C], where the $a=5$ nm, $b=4.3$ nm. The narrowest line width achieved was 130 nm, and the height measured 3.1 nm.

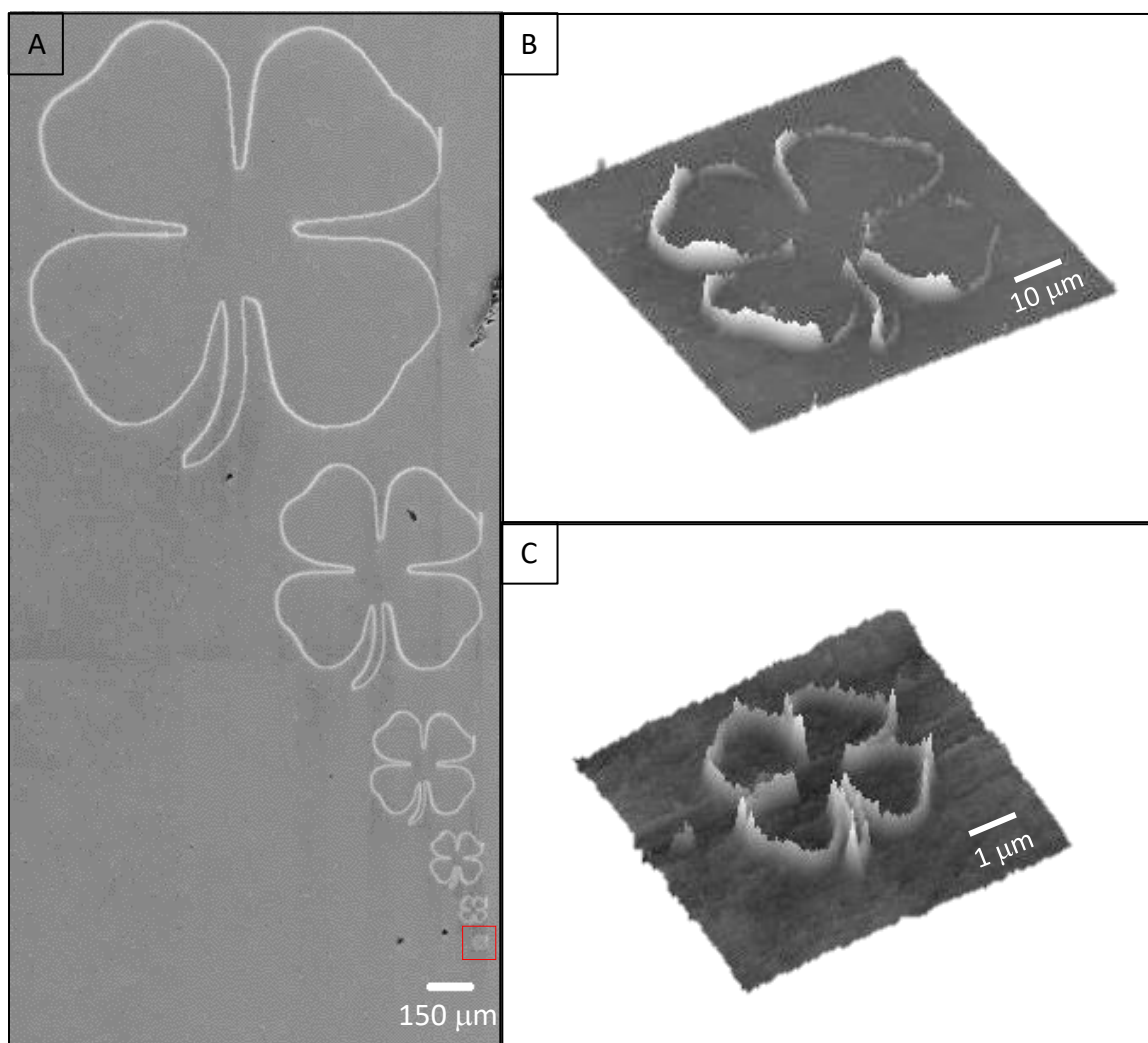


Figure 5-5. [A] SEM image of clovers 1-6 made of Loctite® AA 349™ on a glass slide substrate. [B] 3D display of an AFM topographic image of clover 6 as indicated in the red frame in (A). [C] 3D display of an AFM topographic image of the smallest 3D structure, clover 7.

5.4. Conclusion

Using AFM-based technology and microfluidic probes, we demonstrated the production of 3D hierarchical structures using custom designed architectures. The lateral spatial precision by this method reached 4.8 nm over the 1 mm feature range. A polymer-based material was delivered and cured within xyz seconds/minutes with a light source nearby. The results were reproducible, with heights ranging from 4.8 nm to 6.0 nm for single pass lines and 14 nm to 17 nm for 2 passes lines, with a printing speed of 50 $\mu\text{m/s}$. The robustness of this method was also shown with heights ranging from 3.3 nm to 4.0 nm for single pass lines and 7.5 nm to 11.3 for 2 passes lines when the printing speed was 200 $\mu\text{m/s}$. Since direct writing has advantage of accommodating wide range of materials, work is in progress to producing functional 3D nanostructures and hierarchical 3D structures by design. With the high spatial precision achieved by this approach, we envision a broad range of applications from sensors, nanodevices, tissue engineering to new types of biomaterials.

5.5. Acknowledgements

Most of the work described in this chapter has been submitted to *J. Phys. Chem.*, and currently under review. If accepted, the text and figures can be used with permission from ACS (see url: <http://pubs.acs.org/pb-assets/acspubs/Migrated/dissertation.pdf> for copyright policy). The financial support for this work was provided by Gordon and Betty Moore Foundation, National Science Foundation (CHE-1413745), Conselho Nacional de Desenvolvimento Científico e Tecnológico (Brazilian National Council for Scientific and Technological Development) for providing funds to carry out this work.

CHAPTER 6 ON-GOING AND FUTURE WORK

6.1. Three-Dimensional Display of AFM Stacked Image Layers

AFM has a property of determining the 3D features of a surface and the structures on it. The ability of scanning a surface with a sharp probe enables the determination of the topography of the sample of interest. However, in a process involving multi steps in which the features of a structure are altered, those inner features are no longer “visible” to the AFM scanning probe. The described issue is illustrated in Figure 6-1.

The proposed solution for this issue is to create a macro to be incorporated into IgorPro (Oxford Instruments AFM image acquisition and processing software). The macro consists of a platform where it is possible to overlap multiple AFM images and allow the visualization of all of those layers of images at once in the same display. With such features, multi-layered structures that are imaged in between deposition steps can be put together and all of the inner features of the created structures can be visualized. Preliminary results are shown in Figure 6-2.

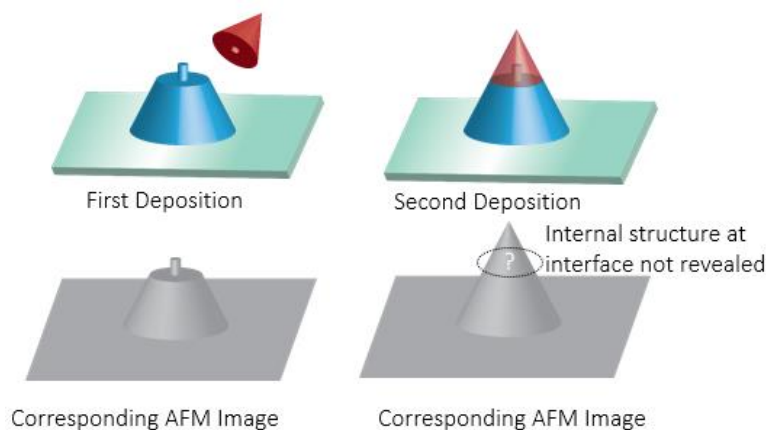


Figure 6-1. Illustration of the issue with multi-layered structures and the absence of inner features information under AFM conventional display methods.

Figure 6-2 shows the AFM topographic images of the structures at 3 different steps and the corresponding images after being processed by the macro. The following step is to overlap those processed images, aligning them with landmarks on the surface. The images will not necessarily cover the exact same area. It is necessary to crop out the areas which are not composed of 3 layers of images for better looking displays.

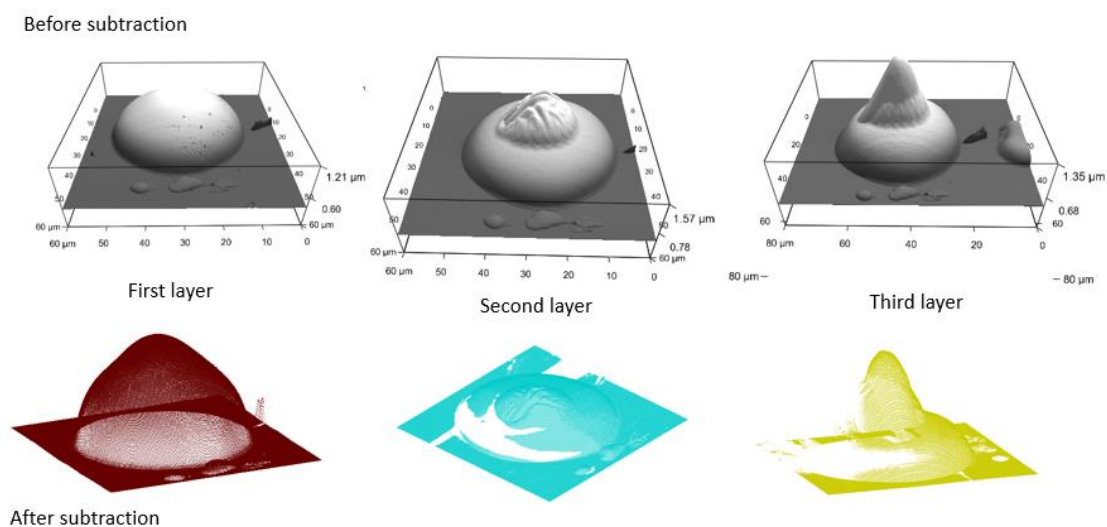


Figure 6-2. Three layered structure imaged in between deposition steps. The first row shows the AFM topographic images of the structures at 3 different steps, while the second row shows the corresponding images after being processed by the macro.

The resulting 3D display is shown in Figure 6-3. In the Figure, it is possible to see the 3 overlapped images with different colors, representing each of the steps of deposition of material and consequently, each of the layers in this structures.

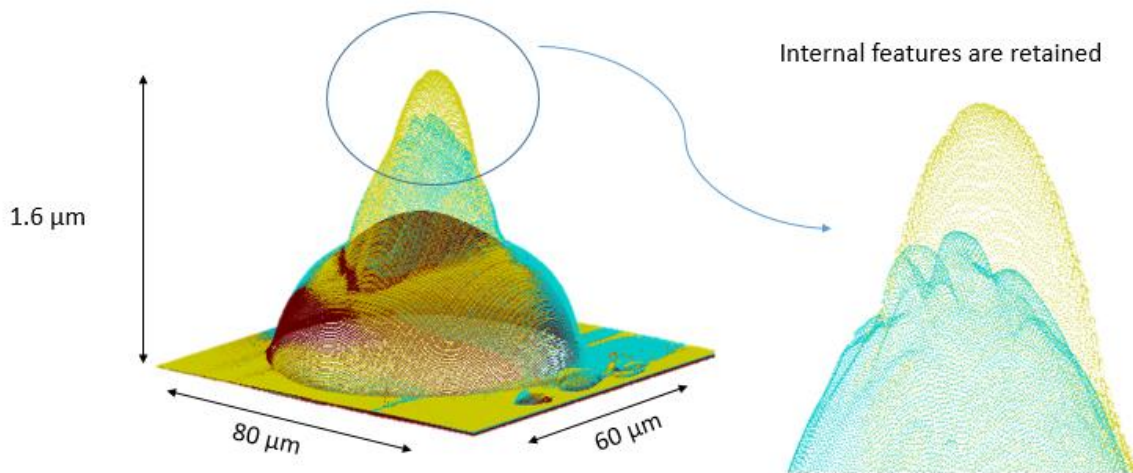


Figure 6-3. Resulting 3D display of the 3 overlapped images, representing the 3 layers of material in this structure. Each layer is represented with a different color in the figure.

With the preliminary results shown in this chapter, the main features (alignment, stacking and transparency) of the software were proven to work with the 3-layered structure. Also, the inner features of the structure could be displayed. The next steps of development of this macro will focus on the automation of the process, which is still mostly manually controlled. The development of an auto-alignment feature is currently under way and will be the next enhancement of the macro. Once this step is accomplished, the focus will be on building a more complex 3D structure with clear designed inner structures. Some efforts have already been made towards this goal, and are shown in Figure 6-4 and 6-5.

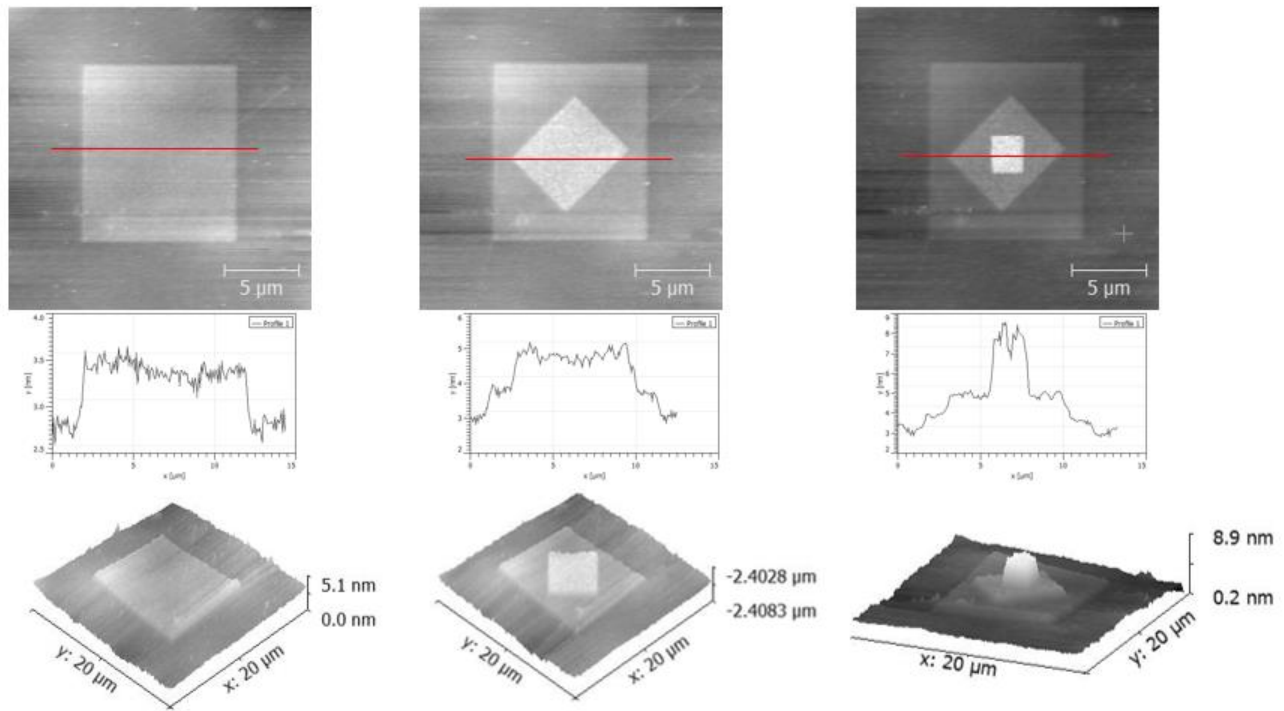


Figure 6-4. AFM topographic images of a three-layered square “pyramid”. The first layer has the largest square as the base and the following squares are systematically smaller and inserted into the base.

Figures 6-4 and 6-5 show the AFM topographic images of three-layered square pyramid structures. The final structure for both cases look alike if shown on their own. The difference between them is in the way they were built. Figure 6-4 shows the pyramid built on a large base with 2 smaller layers deposited on top. Figure 6-5 shows the pyramid built on a small base with 2 larger layers deposited on top. Because of the difference in the fabrication steps, the layers have different shapes when comparing both structures. However, when analyzing the images with the final structures, they look similar to each other.

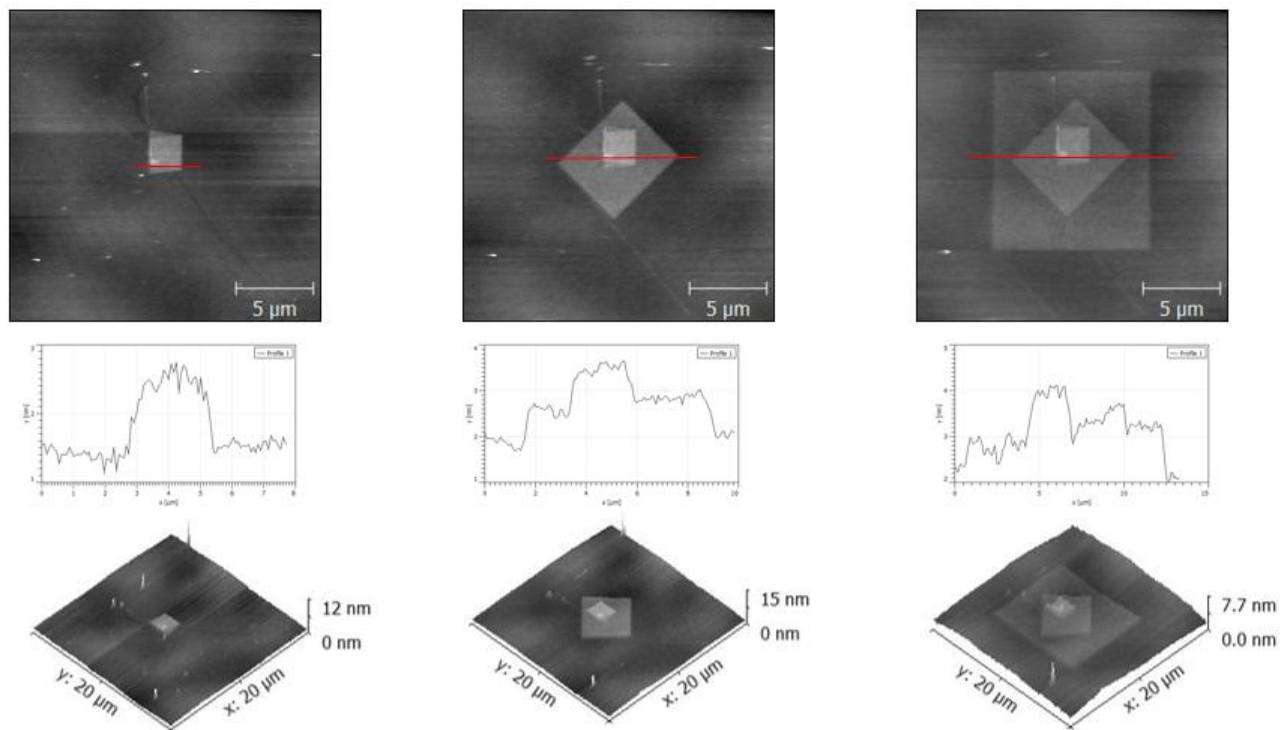


Figure 6-5. AFM topographic images of a three-layered square “pyramid”. The first layer has the smallest square as the base and the following squares are systematically larger and built on top of the base.

The use of the macro, in this case, will make possible to make evident the difference in the shapes of the layers for each of the structures. Although enough to demonstrate the application of the macro, these structures are not the most complete example to be demonstrated. For this reason, one of the next steps of this project is to build multi-layered structures with complex inner features, such as grids, which will better demonstrate all the properties of the developed tool.

6.2. Acknowledgements

The software development was carried out by Mr. William Deng, an undergraduate student who worked under the supervision of my advisors. The financial support for this work was provided by Gordon and Betty Moore Foundation, National Science Foundation (CHE-1413745), Conselho Nacional

de Desenvolvimento Científico e Tecnológico (Brazilian National Council for Scientific and Technological Development) for providing funds to carry out this work.

APPENDIX

A.1. Standard Operation Procedures

A.1.1. Cytosurge FluidFM

A.1.1.1. Experiment Preparation Steps

I) Probe preparation

- Material Filling Aid System

- a. 1 μ L syringe

- b. Check the level of your material in the probe under the microscope

- Probe Placing

Under the tab “Exchange plates”, click on “stage to right port”. That will bring the probe holder on the right port, where you will place your probe on one of the four positions.

- Illumination Set Up

- a. Under the “Settings” tab, click “Bot” and “Illumination”. Set it to 1%.

- b. Still under “Settings” tab, click “View” and set the exposure time to 20 ms and the gain to 100.

- Probe Dropping and Pick Up

Under the tab “Prepare Systems”, select an open spot on the probe holder to drop the current dummy probe and select the position you previously placed the probe to be used in your experiment.

- Probe Sealing Checking

Check the sealing of the probe using the “name” software. Select the “name” sensor and click run. On ARYA software, select the syringe icon on the left menu and apply a pressure of 20 mbar. If the probe is sealed, the sensor will show a spike and then go back to zero (or close to zero). If the probe is not sealed, the sensor will show a pressure greater than zero. In case of bad sealing, reach out to the probe and manually (and gently) adjust its position until you hear a “click”. Repeat the sealing checking.

- Laser Alignment

- a. Still on the “Prepare systems” tab, click on align laser. At this point, remove the IR filter in the microscope. You will be able to see the laser position on the probe.

Manually adjust the position of the laser by changing the x and y positions of the laser.

The laser beam should be placed at the end of the tip of the probe.

- b. Perform the automatic alignment of the laser. You should have a plot like the one showed below as a result of the automatic alignment.

- Probe filling:

- a. Set the reference of your probe.
- b. Apply a pressure for filling up the probe with your material. The more viscous the material you are using, the greater the pressure you should use.
- c. The reference image on the right side will show the evolution of the material on filling the probe.
- d. Release the pressure once the material reaches the very tip of your probe.

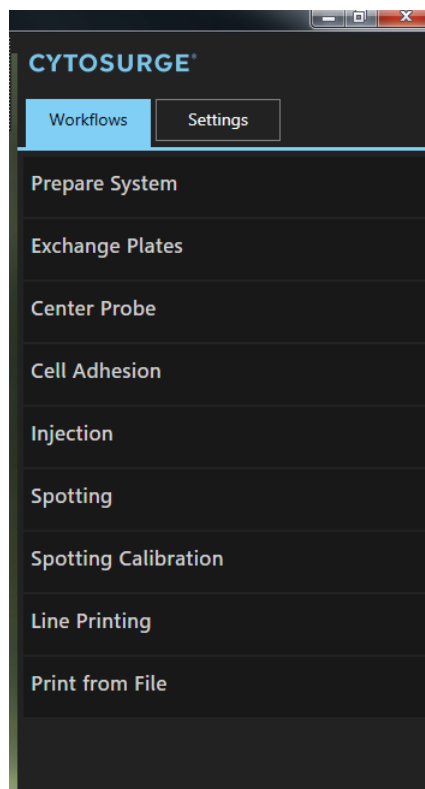
II) Sample Preparation

- Under the tab “Exchange plates”, click on “stage to left port”. Carefully place your sample on the sample holder and clamp it down.

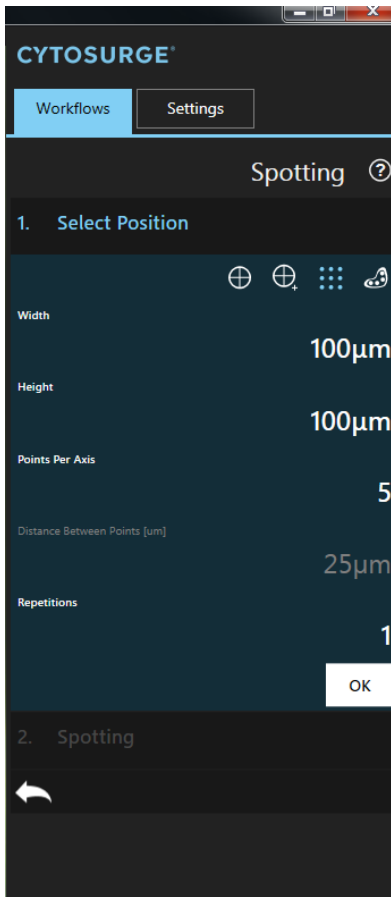
- Position the probe over your sample by clicking the “Eye” icon on the right menu and selecting the spot of your choice on your sample.
- You are ready for your experiment!

A.1.1.2. Spotting

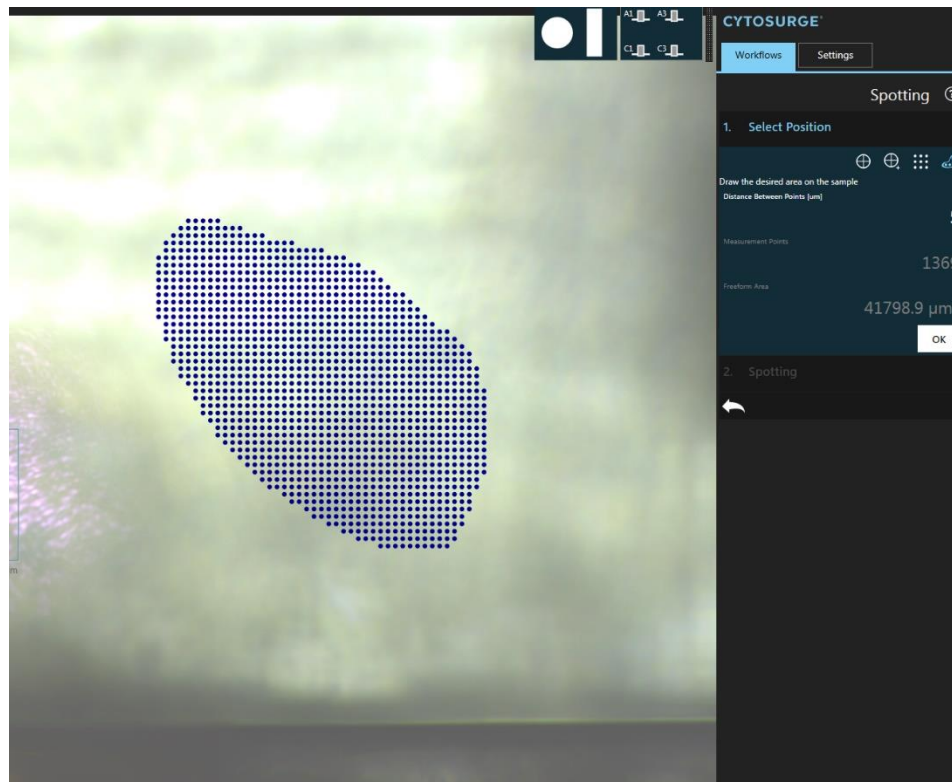
- Fill the probe and go to 20 mbar once the probe is filled. Bring the probe to substrate.
- Go to “workflow”, hit “spotting”



- Now the user can define a grid of points by configuring the number of points per axis and the size of the grid. “Width” defines the length of the grid along x axis. “Height” defines the length of the grid along y axis.



- Under “Free Form”, the user can draw a shape with its finger and the resulting area is filled with the configured distance between points. The field “Measurement points” states how many points were effectively assigned.



- The user can now define the lithography parameter by going to “spotting” under “select position”.

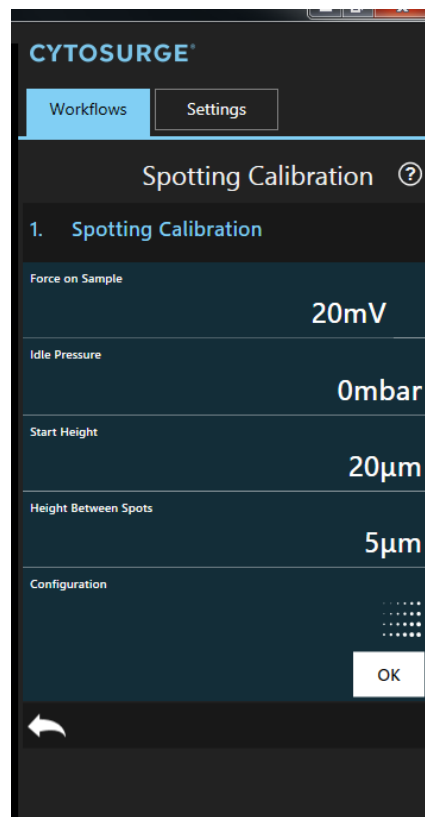


- First, the user can define “Approach Speed” and “Retract Speed”. The spotting pressure and dwelling times are defined by “Pressure” and “Duration”. The “Idle Pressure” is applied between two spots, when the probe is not contact with the surface. The user can use it to keep the probe filled. The “Height between Spots” is the distance between the substrate and the probe when the sample is moving between each time spotting. Finally, how much force the probe applies to the surface while spotting is adjusted with the “Set Point”.
- Press “OK” to start spotting.

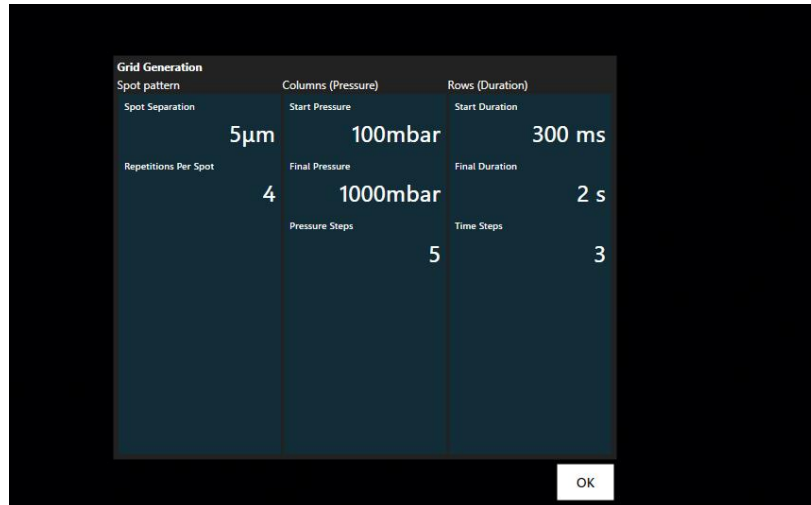
A.1.1.3. Spotting Calibration SOP

The spotting calibration workflow helps the user to achieve the desired spotting results by sweeping the pressure range and dwelling time.

- Go to “workflow”, hit “Spotting Calibration”. It shares many features with “Spotting” workflow, which will not be repeated here. “Force on Sample” is the how much force the probe applies to the surface while spotting. “Start Height” assures that the probe does not touch the surface unintended.



- To set the sweep parameter, click on the grid symbol and the following dialog will pop up.



- Set the following parameters:

Spot separation: The distance between two test spots

Repetitions per spot: How many times the same condition should be printed. The corresponding points will be clustered next to each other.

Start Pressure: The lowest pressure you want to test.

Final Pressure: The highest pressure you want to test.

Pressure Steps: How many different pressures you want to test.

Start Duration: The minimum printing time you want to test.

Final Duration: The maximum printing time you want to test.

Time Steps: How many different printing times you want to test.

The calibration workflow makes spots while sweeping pressure and dwelling time as follows:

- ✓ It calculates all the possible combinations of pressure and pause. If you have, for example, 4 pressures and 7 dwelling times, this gives 28 conditions to test.
- ✓ The necessary area is calculated with the number of repetitions and the spot separation.
- ✓ The grid is automatically generated
- ✓ The workflow can now be started by clicking on “OK”

REFERENCES

1. Zeira, A.; Chowdhury, D.; Hoepfner, S.; Liu, S.; Berson, J.; Cohen, S. R.; Maoz, R.; Sagiv, J., Patterned Organosilane Monolayers as Lyophobic–Lyophilic Guiding Templates in Surface Self-Assembly: Monolayer Self-Assembly versus Wetting-Driven Self-Assembly. *Langmuir* **2009**, *25*, 13984-14001.
2. Liu, M.; Amro, N. A.; Liu, G.-y., Nanografting for Surface Physical Chemistry. *Annu. Rev. Phys. Chem.* **2008**, *59*, 367-386.
3. Liu, J.-F.; Cruchon-Dupeyrat, S.; Garno, J. C.; Frommer, J.; Liu, G.-y., Three-Dimensional Nanostructure Construction via Nanografting: Positive and Negative Pattern Transfer. *Nano Lett.* **2002**, *2*, 937-940.
4. Zhao, J.; Swartz, L. A.; Lin, W.-f.; Schlenoff, P. S.; Frommer, J.; Schlenoff, J. B.; Liu, G.-y., Three-dimensional nanoprinting via scanning probe lithography-delivered layer-by-layer deposition. *ACS Nano* **2016**, *10*, 5656–5662.
5. Edidin, M., Timeline - Lipids on the frontier: a century of cell-membrane bilayers. *Nat Rev Mol Cell Bio* **2003**, *4* (5), 414-418.
6. García-Arribas, A. B.; Busto, J. V.; Alonso, A.; Goni, F. M., Atomic Force Microscopy Characterization of Palmitoylceramide and Cholesterol Effects on Phospholipid Bilayers: A Topographic and Nanomechanical Study. *Langmuir* **2015**, *31*, 3135–3145.
7. Redondo-Morata, L.; Giannotti, M. I.; Sanz, F., Influence of Cholesterol on the Phase Transition of Lipid Bilayers: A Temperature-Controlled Force Spectroscopy Study. *Langmuir* **2012**, *28*, 12851-12860.
8. Frederix, P. L. T. M.; Bosshart, P. D.; Engel, A., Atomic Force Microscopy of Biological Membranes. *Biophys J* **2009**, *96* (2), 329-338.
9. Hansma, H. G.; Hoh, J. H., Biomolecular Imaging with the Atomic-Force Microscope. *Annu Rev Bioph Biom* **1994**, *23*, 115-139.
10. Mingeot-Leclercq, M. P.; Deleu, M.; Brasseur, R.; Dufrene, Y. F., Atomic force microscopy of supported lipid bilayers. *Nat Protoc* **2008**, *3* (10), 1654-1659.
11. El Kirat, K.; Morandat, S.; Dufrene, Y. F., Nanoscale analysis of supported lipid bilayers using atomic force microscopy. *Bba-Biomembranes* **2010**, *1798* (4), 750-765.
12. Darnell, J. E.; Lodish, H. F.; Baltimore, D., *Molecular cell biology*. 2nd ed.; Scientific American Books : Distributed by W.H. Freeman: New York, N.Y., 1990; p xl, 1105 p.

13. Kasahara, K.; Sanai, Y., Involvement of lipid raft signaling in ganglioside-mediated neural function. *Trends Glycosci Glyc* **2001**, *13* (74), 587-594.
14. Stoddart, A.; Dykstra, M. L.; Brown, B. K.; Song, W. X.; Pierce, S. K.; Brodsky, F. M., Lipid rafts unite signaling cascades with clathrin to regulate BCR internalization. *Immunity* **2002**, *17* (4), 451-462.
15. Lingwood, D.; Simons, K., Lipid Rafts As a Membrane-Organizing Principle. *Science* **2010**, *327* (5961), 46-50.
16. Gorter, E.; Grendel, F., On bimolecular layers of lipoids on the chromocytes of the blood. *J Exp Med* **1925**, *41* (4), 439-443.
17. Castellana, E. T.; Cremer, P. S., Solid supported lipid bilayers: From biophysical studies to sensor design. *Surf Sci Rep* **2006**, *61* (10), 429-444.
18. Bayerl, T. M.; Bloom, M., Physical-Properties of Single Phospholipid-Bilayers Adsorbed to Micro Glass-Beads - a New Vesicular Model System Studied by H-2-Nuclear Magnetic-Resonance. *Biophys J* **1990**, *58* (2), 357-362.
19. Johnson, S. J.; Bayerl, T. M.; Mcdermott, D. C.; Adam, G. W.; Rennie, A. R.; Thomas, R. K.; Sackmann, E., Structure of an Adsorbed Dimyristoylphosphatidylcholine Bilayer Measured with Specular Reflection of Neutrons. *Biophys J* **1991**, *59* (2), 289-294.
20. Lambacher, A.; Fromherz, P., Fluorescence interference-contrast microscopy on oxidized silicon using a monomolecular dye layer. *Appl Phys a-Mater* **1996**, *63* (3), 207-216.
21. Tanaka, M.; Sackmann, E., Supported membranes as biofunctional interfaces and smart biosensor platforms. *Phys Status Solidi A* **2006**, *203* (14), 3452-3462.
22. Sinner, E. K.; Knoll, W., Functional tethered membranes. *Curr Opin Chem Biol* **2001**, *5* (6), 705-711.
23. Budvytyte, R.; Valincius, G.; Niaura, G.; Voiciuk, V.; Mickevicius, M.; Chapman, H.; Goh, H. Z.; Shekhar, P.; Heinrich, F.; Shenoy, S.; Losche, M.; Vanderah, D. J., Structure and Properties of Tethered Bilayer Lipid Membranes with Unsaturated Anchor Molecules. *Langmuir* **2013**, *29* (27), 8645-8656.
24. Shenoy, S.; Moldovan, R.; Fitzpatrick, J.; Vanderah, D. J.; Deserno, M.; Losche, M., In-plane homogeneity and lipid dynamics in tethered bilayer lipid membranes (tBLMs). *Soft Matter* **2010**, *6* (6), 1263-1274.
25. Heinrich, F.; Ng, T.; Vanderah, D. J.; Shekhar, P.; Mihailescu, M.; Nanda, H.; Losche, M., A New Lipid Anchor for Sparsely Tethered Bilayer Lipid Membranes. *Langmuir* **2009**, *25* (7), 4219-4229.

26. McGillivray, D. J.; Valincius, G.; Heinrich, F.; Robertson, J. W. F.; Vanderah, D. J.; Febo-Ayala, W.; Ignatjev, I.; Losche, M.; Kasianowicz, J. J., Structure of Functional Staphylococcus aureus alpha-Hemolysin Channels in Tethered Bilayer Lipid Membranes. *Biophys J* **2009**, *96* (4), 1547-1553.
27. Langmuir, I., The constitution and fundamental properties of solids and liquids. II. Liquids. *J Am Chem Soc* **1917**, *39*, 1848-1906.
28. Blodgett, K. B., Films built by depositing successive monomolecular layers on a solid surface. *J Am Chem Soc* **1935**, *57* (1), 1007-1022.
29. Kienle, D. F.; de Souza, J. V.; Watkins, E. B.; Kuhl, T. L., Thickness and refractive index of DPPC and DPPE monolayers by multiple-beam interferometry. *Anal Bioanal Chem* **2014**, *406* (19), 4725-4733.
30. Marra, J.; Israelachvili, J., Direct Measurements of Forces between Phosphatidylcholine and Phosphatidylethanolamine Bilayers in Aqueous-Electrolyte Solutions. *Biochemistry-US* **1985**, *24* (17), 4608-4618.
31. Tamm, L. K.; McConnell, H. M., Supported Phospholipid-Bilayers. *Biophys J* **1985**, *47* (1), 105-113.
32. Watkins, E. B.; Miller, C. E.; Mulder, D. J.; Kuhl, T. L.; Majewski, J., Structure and Orientational Texture of Self-Organizing Lipid Bilayers. *Phys Rev Lett* **2009**, *102* (23).
33. Cremer, P. S.; Boxer, S. G., Formation and spreading of lipid bilayers on planar glass supports. *J Phys Chem B* **1999**, *103* (13), 2554-2559.
34. Bunjes, N.; Schmidt, E. K.; Jonczyk, A.; Rippmann, F.; Beyer, D.; Ringsdorf, H.; Graber, P.; Knoll, W.; Naumann, R., Thiopeptide-supported lipid layers on solid substrates. *Langmuir* **1997**, *13* (23), 6188-6194.
35. Salamon, Z.; Wang, Y.; Tollin, G.; Macleod, H. A., Assembly and Molecular-Organization of Self-Assembled Lipid Bilayers on Solid Substrates Monitored by Surface-Plasmon Resonance Spectroscopy. *Bba-Biomembranes* **1994**, *1195* (2), 267-275.
36. Orozco-Alcaraz, R.; Kuhl, T. L., Interaction Forces between DPPC Bilayers on Glass. *Langmuir* **2013**, *29* (1), 337-343.
37. Watkins, E. B.; Miller, C. E.; Liao, W. P.; Kuhl, T. L., Equilibrium or Quenched: Fundamental Differences between Lipid Monolayers, Supported Bilayers, and Membranes. *Acs Nano* **2014**, *8* (4), 3181-3191.
38. Lee, K. Y. C.; Lipp, M. M.; Takamoto, D. Y.; Ter-Ovanesyan, E.; Zasadzinski, J. A.; Waring, A. J., Apparatus for the continuous monitoring of surface morphology via fluorescence microscopy during monolayer transfer to substrates. *Langmuir* **1998**, *14* (9), 2567-2572.

39. Girard-Egrot, A. P.; Blum, L. J., Langmuir-Blodgett Technique for Synthesis of Biomimetic Lipid Membranes. In *Nanobiotechnology of Biomimetic Membranes*, Martin, D. K., Ed. Springer US: Boston, MA, 2007; pp 23-74.
40. Langmuir, I.; Schaefer, V. J., Activities of urease and pepsin monolayers. *J Am Chem Soc* **1938**, *60*, 1351-1360.
41. Hughes, A. V.; Goldar, A.; Gerstenberg, M. C.; Roser, S. J.; Bradshaw, J., A hybrid SAM phospholipid approach to fabricating a free supported lipid bilayer. *Phys Chem Chem Phys* **2002**, *4* (11), 2371-2378.
42. Liu, J.; Conboy, J. C., 1,2-diacyl-phosphatidylcholine flip-flop measured directly by sum-frequency vibrational spectroscopy. *Biophys J* **2005**, *89* (4), 2522-2532.
43. Anglin, T. C.; Conboy, J. C., Lateral pressure dependence of the phospholipid transmembrane diffusion rate in planar-supported lipid bilayers. *Biophys J* **2008**, *95* (1), 186-193.
44. Anglin, T. C.; Cooper, M. P.; Li, H.; Chandler, K.; Conboy, J. C., Free Energy and Entropy of Activation for Phospholipid Flip-Flop in Planar Supported Lipid Bilayers. *J Phys Chem B* **2010**, *114* (5), 1903-1914.
45. Gerelli, Y.; Porcar, L.; Fragneto, G., Lipid Rearrangement in DSPC/DMPC Bilayers: A Neutron Reflectometry Study. *Langmuir* **2012**, *28* (45), 15922-15928.
46. Wacklin, H. P.; Thomas, R. K., Spontaneous formation of asymmetric lipid bilayers by adsorption of vesicles. *Langmuir* **2007**, *23* (14), 7644-7651.
47. Reimhult, E.; Hook, F.; Kasemo, B., Intact vesicle adsorption and supported biomembrane formation from vesicles in solution: Influence of surface chemistry, vesicle size, temperature, and osmotic pressure. *Langmuir* **2003**, *19* (5), 1681-1691.
48. Reviakine, I.; Brisson, A., Formation of supported phospholipid bilayers from unilamellar vesicles investigated by atomic force microscopy. *Langmuir* **2000**, *16* (4), 1806-1815.
49. Goksu, E. I.; Vanegas, J. M.; Blanchette, C. D.; Lin, W. C.; Longo, M. L., AFM for structure and dynamics of biomembranes. *Bba-Biomembranes* **2009**, *1788* (1), 254-266.
50. Morigaki, K.; Tawa, K., Vesicle fusion studied by surface plasmon resonance and surface plasmon fluorescence spectroscopy. *Biophys J* **2006**, *91* (4), 1380-1387.
51. Kalb, E.; Frey, S.; Tamm, L. K., Formation of Supported Planar Bilayers by Fusion of Vesicles to Supported Phospholipid Monolayers. *Biochim Biophys Acta* **1992**, *1103* (2), 307-316.
52. Crane, J. M.; Kiessling, V.; Tamm, L. K., Measuring lipid asymmetry in planar supported bilayers by fluorescence interference contrast microscopy. *Langmuir* **2005**, *21* (4), 1377-1388.

53. Sugihara, K.; Jang, B.; Schneider, M.; Voros, J.; Zambelli, T., A universal method for planar lipid bilayer formation by freeze and thaw. *Soft Matter* **2012**, *8* (20), 5525-5531.
54. Seul, M.; Sammon, M. J., Preparation of Surfactant Multilayer Films on Solid Substrates by Deposition from Organic Solution. *Thin Solid Films* **1990**, *185* (2), 287-305.
55. Mennicke, U.; Salditt, T., Preparation of solid-supported lipid bilayers by spin-coating. *Langmuir* **2002**, *18* (21), 8172-8177.
56. Simonsen, A. C.; Bagatolli, L. A., Structure of spin-coated lipid films and domain formation in supported membranes formed by hydration. *Langmuir* **2004**, *20* (22), 9720-9728.
57. Unsay, J. D.; Cosentino, K.; Garcia-Saez, A. J., Atomic Force Microscopy Imaging and Force Spectroscopy of Supported Lipid Bilayers. *Jove-J Vis Exp* **2015**, (101).
58. Garcia, R.; Perez, R., Dynamic atomic force microscopy methods. *Surf Sci Rep* **2002**, *47* (6-8), 197-301.
59. Howells, S.; Chen, T.; Gallagher, M.; Yi, L.; Sarid, D., Enhanced Effects with Scanning Force Microscopy. *J Appl Phys* **1991**, *69* (10), 7330-7332.
60. Picas, L.; Milhiet, P.-E.; Hernández-Borrell, J., Atomic force microscopy: A versatile tool to probe the physical and chemical properties of supported membranes at the nanoscale. *Chemistry and Physics of Lipids* **2012**, *165*, 845-860.
61. Merkel, R.; Nassoy, P.; Leung, A.; Ritchie, K.; Evans, E., Energy landscapes of receptor-ligand bonds explored with dynamic force spectroscopy. *Nature* **1999**, *397* (6714), 50-53.
62. Lee, G. U.; Kidwell, D. A.; Colton, R. J., Sensing Discrete Streptavidin Biotin Interactions with Atomic-Force Microscopy. *Langmuir* **1994**, *10* (2), 354-357.
63. Moy, V. T.; Florin, E. L.; Gaub, H. E., Intermolecular Forces and Energies between Ligands and Receptors. *Science* **1994**, *266* (5183), 257-259.
64. Benz, M.; Gutsman, T.; Chen, N. H.; Tadmor, R.; Israelachvili, J., Correlation of AFM and SFA measurements concerning the stability of supported lipid bilayers. *Biophys J* **2004**, *86* (2), 870-879.
65. Dufrene, Y. F.; Barger, W. R.; Green, J. B. D.; Lee, G. U., Nanometer-scale surface properties of mixed phospholipid monolayers and bilayers. *Langmuir* **1997**, *13* (18), 4779-4784.
66. Bassereau, P.; Pincet, F., Quantitative analysis of holes in supported bilayers providing the adsorption energy of surfactants on solid substrate. *Langmuir* **1997**, *13* (26), 7003-7007.
67. Rinia, H. A.; Demel, R. A.; van der Eerden, J. P. J. M.; de Kruijff, B., Blistering of Langmuir-Blodgett bilayers containing anionic phospholipids as observed by atomic force microscopy. *Biophys J* **1999**, *77* (3), 1683-1693.

68. Leckband, D. E.; Schmitt, F. J.; Israelachvili, J. N.; Knoll, W., Direct Force Measurements of Specific and Nonspecific Protein Interactions. *Biochemistry-Us* **1994**, *33* (15), 4611-4624.
69. Leckband, D. E.; Helm, C. A.; Israelachvili, J., Role of Calcium in the Adhesion and Fusion of Bilayers. *Biochemistry-Us* **1993**, *32* (4), 1127-1140.
70. Kurniawan, J.; Yin, N. N.; Liu, G. Y.; Kuhl, T. L., Interaction Forces between Ternary Lipid Bilayers Containing Cholesterol. *Langmuir* **2014**, *30* (17), 4997-5004.
71. Kurniawan, J.; Kuhl, T. L., Characterization of Solid-Supported Dipalmitoylphosphatidylcholine Membranes Containing Cholesterol. *Langmuir* **2015**, *31* (8), 2527-2532.
72. Jung, S. Y.; Holden, M. A.; Cremer, P. S.; Collier, C. P., Two-component membrane lithography via lipid backfilling. *Chemphyschem* **2005**, *6* (3), 423-426.
73. Schlogl, S.; Reischl, M.; Ribitsch, V.; Kern, W., UV induced microcellular foaming-A new approach towards the production of 3D structures in offset printing techniques. *Progress in Organic Coatings* **2012**, *73* (1), 54-61.
74. Chien, K. B.; Makridakis, E.; Shah, R. N., Three-dimensional printing of soy protein scaffolds for tissue regeneration. *Tissue Engineering Part C - Methods* **2013**, *19* (6), 417-426.
75. Braunschweig, A. B.; Huo, F.; Mirkin, C. A., Molecular printing. *Nat Chem* **2009**, *1*, 353-358.
76. Ginger, D. S.; Zhang, H.; Mirkin, C. A., The Evolution of Dip-Pen Nanolithography. *Angew. Chem. Int. Ed.* **2004**, *43*, 30-45.
77. Garcia, R.; Knoll, A. W.; Riedo, E., Advanced scanning probe lithography. *Nat Nano* **2014**, *9*, 577-587.
78. Radha, B.; Liu, G. L.; Eichelsdoerfer, D. J.; Kulkarni, G. U.; Mirkin, C. A., Layer-by- Layer Assembly of a Metallomesogen by Dip-Pen Nanolithography. *ACS Nano* **2013**, *7*, 2602-2609.
79. Pires, D.; Hedrick, J. L.; De Silva, A.; Frommer, J.; Gotsmann, B.; Wolf, H.; Despont, M.; Duerig, U.; Knoll, A. W., Nanoscale Three-Dimensional Patterning of Molecular Resists by Scanning Probes. *Science* **2010**, *328*, 732-735.
80. Drexler, C. I.; Moore, K. B.; Causey, C. P.; Mullen, T. J., Atomic Force Microscopy Characterization and Lithography of Cu-Ligated Mercaptoalkanoic Acid "Molecular Ruler" Multilayers. *Langmuir* **2014**, *30*, 7447-7455.
81. Lee, S. W.; Sanedrin, R. G.; Oh, B. K.; Mirkin, C. A., Nanostructured Polyelectrolyte Multilayer Organic Thin Films Generated via Parallel Dip-Pen Nanolithography. *Adv. Mater.* **2005**, *17*, 2749-2753.

82. Albrecht, K.; Pernites, R.; Felipe, M. J.; Advincula, R. C.; Yamamoto, K., Patterning Carbazole-Phenylazomethine Dendrimer Films. *Macromolecules* **2012**, *45*, 1288-1295.
83. Park, J. Y.; Taranekar, P.; Advincula, R., Polythiophene Precursor Electrochemical Nanolithography: Highly Local Thermal and Morphological Characterization. *Soft Matter* **2011**, *7*, 1849-1855.
84. Zhang, X.; Jiang, X. N.; Sun, C., Micro-stereolithography of polymeric and ceramic microstructures. *Sens. Actuators A Phys.* **1999**, *77*, 149-156.
85. Smay, J. E.; Cesarano III, J.; Lewis, J. A., Colloidal inks for directed assembly of 3D periodic structures. *Langmuir* **2002**, *18*, 5429-5437.
86. Gratson, G. M.; Xu, M.; Lewis, J. A., Direct writing of threedimensional webs. *Nature* **2004**, *428*, 386.
87. Gratson, G. M.; Garcia-Santamaria, F.; Lousse, V.; Xu, M.; Fan, S.; Lewis, J. A.; Braun, P. V., Direct-write assembly of three-dimensional photonic crystals: conversion of polymer scaffolds to silicon hollow-woodpile structures. *Adv. Mater.* **2006**, *18*, 461-465.
88. Therriault, D.; Shepherd, R. F.; White, S. R.; Lewis, J. A., Fugitive inks for direct-write assembly of three-dimensional microvascular networks. *Adv. Mater.* **2005**, *17*, 395-399.
89. Lewis, J. A., Direct ink writing of 3D functional materials. *Adv. Funct. Mater.* **2006**, *16*, 2193-2204.
90. Ahn, B. Y.; Duoss, E. B.; Motala, M. J.; Guo, X.; Park, S.-I.; Xiong, Y.; Yoon, J.; Nuzzo, R. G.; Rogers, J. A.; Lewis, J. A., Omnidirectional printing of flexible, stretchable, and spanning silver microelectrodes. *Science* **2009**, *323*, 1590-1593.
91. Schaedler, T. A.; Jacobsen, A. J.; Torrents, A.; Sorensen, A. E.; Lian, J.; Greer, J. R.; Valdivit, L.; Carter, W. B., Ultralight Metallic Microlattices. *Science* **2011**, *334*, 962-965.
92. Zheng, X.; Smith, W.; Jackson, J.; Moran, B.; Cui, H.; Chen, D.; Ye, J.; Fang, N.; Rodriguez, N.; Weisgraber, T.; Spadaccini, C. M., Multiscale metallic metamaterials. *Nature Materials* **2016**, *15*, 1100-1107.
93. Rohrig, M.; Thiel, M.; Worgull, M.; Holscher, H., 3D direct laser writing of nano- and microstructured hierarchical gecko-mimicking surfaces. *Small* **2012**, *8*, 3009-3015.
94. Ivanova, O.; Williams, C.; Campbell, T., Additive manufacturing (AM) and nanotechnology: promises and challenges. *Rapid Prototyp. J.* **2013**, *19*, 353-364.
95. Jang, D.; Meza, L. R.; Greer, F.; Greer, J. R., Fabrication and deformation of three-dimensional hollow ceramic nanostructures. *Nat. Mater.* **2013**, *12*, 893-898.

96. Frazier, W. E., Metal additive manufacturing: a review. *J. Mater. Eng. Perform.* **2014**, *23*, 1917-1928.
97. Farahani, R. D.; Chizari, K.; Therriault, D., Three-dimensional printing of freeform helical microstructures: a review. *Nanoscale* **2014**, *6*, 10470-10485.
98. Sachs, E.; Cima, M.; Williams, P.; Brancazio, D.; Cornie, J., Three dimensional printing: rapid tooling and prototypes directly from a CAD mode. *J. Eng. Ind. Trans. ASME* **1992**, *114*, 481-488.
99. Song, J. H.; Edirisinghe, M. J.; Evans, J. R. G., Formulation and multilayer jet printing of ceramic inks. *J. Am. Ceram. Soc.* **1999**, *82*, 3374-3380.
100. Tay, B. Y.; Edirisinghe, M. J., Investigation of some phenomena occurring during continuous ink-jet printing of ceramics. *J. Mater. Res.* **2001**, *16*, 373-384.
101. Seerden, K. A. M.; Reis, N.; Evans, J. R. G.; Grant, P. S.; Halloran, J. W.; Derby, B., Ink-jet printing of wax-based alumina suspensions. *J. Am. Ceram. Soc.* **2001**, *84*, 2514-2520.
102. Mott, M.; Evans, J. R. G., Zirconia/alumina functionally graded material made by ceramic ink jet printing. *Mater. Sci. Eng. A* **1999**, *271*, 344-352.
103. Li, P.; Zong, Y.; Zhang, Y.; Yang, M.; Zhang, R.; Li, S.; Wei, F., In situ fabrication of depth-type hierarchical CNT/quartz fiber filters for high efficiency filtration of sub-micron aerosols and high water repellency. *Nanoscale* **2013**, *5*, 3367-3372.
104. Yablonovitch, E., Inhibited spontaneous emission in solid-state physics and electronics. *Phys. Rev. Lett.* **1987**, *58*, 2059-2062.
105. Joannopoulos, J. D.; Villeneuve, P. R.; Fan, S., Photonic crystals: putting a new twist on light. *Nature* **1997**, *386*, 143-149.
106. Lin, S. Y.; Fleming, J. G.; Hetherington, D. L.; Smith, B. K.; Biswas, R.; Ho, K. M.; Sigalas, M. M.; Zubrzycki, W.; Kurtz, S. R.; Bur, J., A three-dimensional photonic crystal operating at infrared wavelengths. *Nature* **1998**, *394*, 251-253.
107. Yablonovitch, E., Photonic crystals: semiconductors of light. *Sci. Am.* **2001**, *285*, 47-55.
108. Nagel, R. D.; Haeberle, T.; Schmidt, M.; Lugli, P.; Scarpa, G., Large area nano-transfer printing of sub-50-nm metal nanostructures using low-cost semi-flexible hybrid templates. *Nanoscale* **2016**, *11*, 143-151.
109. Melinte, G.; Moldovan, S.; Hirlimann, C.; Liu, X.; Begin-Colin, S.; Begin, D.; Banhart, F.; Pham-Huu, C.; Ersen, O., Towards nanoprinting with metals on graphene. *Nature Comm.* **2015**, *6*, 8071-8078.
110. Pi, H.; Tong, J.; Bian, C.; Xia, S., 3D printed micro/nanofluidic preconcentrator for charged sample based on ion concentration polarization. *J. Micromech. Microeng.* **2017**, *27*, 55008-55015.

111. Park, J.; Kim, K.; Kim, K.; Kim, D.; Cho, D.; Lee, J. H.; Jeon, S., Rapid, high-resolution 3D interference printing of multilevel ultralong nanochannel arrays for high throughput nanofluidic transport. *Adv. Mater.* **2015**, *27*, 8000–8006.
112. Compton, B. G.; Lewis, J. A., 3D-printing of lightweight cellular composites. *Adv. Mater.* **2014**, *26*, 5930-5935.
113. Chai, G. S.; Yoon, S. B.; Yu, J.-S.; Choi, J.-H.; Sung, Y.-E., Ordered porous carbons with tunable pore sizes as catalyst supports in direct methanol fuel cell. *J. Phys. Chem. B* **2004**, *108*, 7074-7079.
114. Zheng, X.; Lee, H.; Weisgraber, T. H.; Shusteff, M.; DeOtte, J.; Duoss, E. B.; Kuntz, J. D.; Biener, M. M.; Ge, Q.; Jackson, J. A.; Kucheyev, S. O.; Fang, N. X.; Spadaccini, C. M., Ultralight, ultrastiff mechanical metamaterials. *Science* **2014**, *344*, 1373-1377.
115. Moorthy, J.; Beebe, D. J., In situ fabricated porous filters for microsystems. *Lab Chip* **2003**, *3*, 62-66.